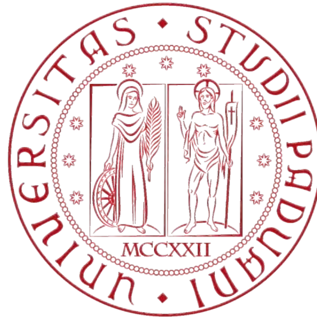

Università degli Studi di Padova
Dipartimento di Ingegneria Industriale
Tesi di Laurea Magistrale in Ingegneria dei Materiali

Realization and Preliminary Operation Tests of AlN-based Piezoelectric Cantilever for Kinetic Energy Harvesting

Laureando:
Matteo Fiorindo

Relatore:
Prof. Daniele Desideri

Anno accademico 2015/2016

To all the people that helped me,
along my way.

Abstract

The aim of this work is the realization and the preliminary tests of a piezoelectric energy harvester.
The piezoelectric material used in the cantilever is aluminum nitride, obtained by reactive magnetron sputtering.
The cantilever is made by a multilayer system based on an aluminum or copper sheet substrate with four layers above, respectively: aluminum, aluminum nitride, Kapton® adhesive tape and aluminum adhesive tape.

Sommario

Lo scopo di questo lavoro è la realizzazione e i test preliminari di un raccoglitore di energia piezoelettrico.
Il materiale piezoelettrico utilizzato nel cantilever è nitruro di alluminio, ottenuto per magnetron sputtering reattivo.
Il cantilever è composto da un sistema multistrato basato su un substrato di lamiera di alluminio o rame, con sopra altri quattro strati, rispettivamente di alluminio, nitruro di alluminio, nastro adesivo in Kapton® e nastro adesivo di alluminio.

Contents

1 Introduction **1**

2 Elements of Crystallography **3**
2.1 Introduction . . . 3
2.2 Crystal lattice . . . 3
2.3 Symmetry groups . . . 4
2.4 Bravais lattices . . . 5
2.5 Miller indices . . . 6

3 Piezoelectricity **9**
3.1 Introduction . . . 9
3.2 Piezoelectric Effect . . . 10
3.2.1 Direct Piezoelectric Effect . . . 12
3.2.2 Converse Piezoelectric Effect . . . 13
3.2.3 Linear Piezoelectric Material . . . 13
3.3 Aluminum Nitride . . . 15
3.3.1 Properties of Aluminum Nitride . . . 15
3.3.2 Piezoelectric Properties of Aluminum Nitride . . . 15
3.3.3 Synthesis of Aluminum Nitride . . . 16

4 Thin Film Deposition Techniques **17**
4.1 Chemical Vapor Deposition . . . 17
4.2 Physical Vapor Deposition . . . 18
4.2.1 Magnetron Sputtering . . . 19
4.3 Thin Film Formation . . . 24

5 Kinetic Energy Harvesting **25**
5.1 Kinetic-to-Electrical Energy Conversion . . . 25
5.2 Electromechanical Model . . . 26
5.3 Cantilever Beam . . . 29
5.3.1 Effect of Deposition of Thin Film . . . 30
5.3.2 Comsol Multiphysics Analysis . . . 31

6 Realization **33**
6.1 Thin Film Deposition Equipment . . . 34
6.2 Realization of the Substrate . . . 37

6.2.1 Preparation of the Substrate for the Deposition 37
6.2.2 Pre-sputtering Phase 39
6.2.3 First Substrate 39
6.2.4 Second Substrate 41
6.2.5 Third Substrate 42
6.2.6 Fourth Substrate 43
6.2.7 Fifth Substrate 46
6.2.8 Sixth Substrate 47
6.3 Realization of the Cantilevers 50

7 First Operation Tests **53**
7.1 Test of a Commercial Cantilever 58
7.2 Analysis of the Second and Third Copper-based Cantilever 58

8 Conclusions **61**

Chapter 1

Introduction

In these years we are facing a continuous increase of the computing power of portable devices and a miniaturization of sensors, allowing the creation of a network of sensors, actuators and portable devices, like smartphones and tablet, in the so-called *Internet of Things*. The sensing devices can be applied to a lot of things, like shoes, clothes or automobiles, but one of the biggest challenges is the energy feeding of all this electronics.
A promising way to get all the required energy, to create a sort of self-feeding sensors, is the use of kinetic energy harvesters. These devices are used to convert mechanical energy, in the form of vibrations, into electrical energy.
Among the kinetic energy harvesters, a type that does not require an external energy feeding to work and that is sufficiently efficient and miniaturizable is the piezoelectric one.
At the moment of writing this thesis, one of the most effective piezoelectric materials is PZT. PZT stands for lead zirconte titanate and, therefore it contains lead, that is higly toxic and polluting. A purpose for research activity on this field is the development of non-toxic materials, with the same characteristics of PZT.
A promising alternative to PZT seems to be aluminum nitride, AlN, that is non-toxic and non-polluting. Furthermore AlN is already being used and studied for the fabrication of sensors and actuators, surface acoustic wave devices [1] and *MEMS* [2, 3, 4]
In the laboratory of Micro and Nanodevices of the Department of Industrial Engineering at the University of Padua, AlN thin film deposition with magnetron sputtering has been sperimented on different substrates. The expertise gained in this kind of deposition guarantees a good starting point for the realization of a piezoelectric cantilever for kinetic energy harvesting.
In this thesis work will be presented the crystallographic theory of piezoelectric materials, the working principles of magnetron sputtering and the realization of the piezoelectric cantilever, with the first operative tests.

Chapter 2

Elements of Crystallography

2.1 Introduction

To understand how a piezoelectric cantilever works it is necessary to start from the basis of crystallography. The solid state of aggregation of matter, differently from gaseous and liquid, shows small atomic separation with strong atom interactions so they are able to move only from fixed positions relative to others by small amplitude vibrations. This interactions give solids rigidity, fixed shape and mechanical strength.
In the solid state the matter can be arranged in amorphous solids or crystal solids.

- Amorphous solids have a disordered arrangement of particles. This causes the anisotropy of the material, which shows the same properties in every direction. Another important property is the absence of a well-defined melting point, substituted with a softening point, i.e. the temperature at which the specific volume shows a variation in the slope.

- Crystal solids are instead characterized by an ordered structure of the particles. As a consequence, crystals have properties that vary along different direction, being called anisotropic materials.
  Another characteristic is the presence of a well defined melting point, at which the structure collapses from the solit state to the liquid state.

2.2 Crystal lattice

A crystal is composed by atoms or molecules arranged in a regular and orderly repeating pattern. The idea that a crystal is made by regular repetition of identical unities arrives from ancient times. Auguste Bravais (1811 – 1863) studied the ordered arrays of atoms, and demonstrated that the pattern of a crystal can be described in terms of unit cell and that there are only a few different kinds of space lattices, i.e. the possible sortings to fill completely the whole space, dividing it in equal volumes [5]. Solids that are made by a single crystal are quite rare; the

remainig crystalline solids are polycrystalline solids, since they are made of many small crystals, called crystallites.
The regular arrangement of single crystals can be represented by a mathematical model, known as space lattice or *Bravais lattice*, which allows to identify all the points of the lattice from the vector

$$\mathbf{a_{123}} = n_1\mathbf{a_1} + n_2\mathbf{a_2} + n_3\mathbf{a_3} \tag{2.1}$$

applied to a starting point O, where $\mathbf{a_1}$, $\mathbf{a_2}$ and $\mathbf{a_3}$ are three translation non-coplanar vectors and n_1, n_2 and n_3 are three arbitrary integers.
In this way it is obtained an infinite periodical repetition, and for any choice of position vector $\mathbf{a_{123}}$, the lattice looks exactly the same.
In an *ideal crystal*, each point of the crystal lattice corresponds to a *basis* or *motif*, i.e. the building block of the crystal, which is a group of atoms, molecules and/or ions.
In the Bravais lattice, the translation vectors of eq.(2.1) identify a parallelepiped, called *primitive cell*, which is not unique. A cell can fill all the space, without being a primitive cell. This difference is related to the number of lattice points that belong to it, taking into account that the points on the sides or the corners are shared with other cells. A cell can be called *primitive* only if it contains only one lattice point. Therefore, all the primitive cells have the same volume. This is the minimum volume for a cell that, with suitable translations, fills all the space.
The volume V_c of a primitive cell can be calculated as

$$V_c = |\mathbf{a_1} \cdot \mathbf{a_2} \times \mathbf{a_3}| \tag{2.2}$$

Since each point of the Bravais lattice corresponds to a basis, and each Bravais point corresponds to a primitive cell, the basis associated to a primitive cell is the minimum group of atoms and/or molecules and/or ions to give a regular space-filling tessellation. In this way the crystal structure can be described with a lattice and a basis [6].

2.3 Symmetry groups

In mathematics, a *symmetry* is an invertible mapping of a system into itself, leaving some property invariant. *Symmetry groups* are therefore a very useful way to describe structures in physical systems. Symmetry operations applied to a single point that maps the lattice into itself are called *point symmetry operations*. A *point group* is a set of point symmetry operations.
The symmetry operations that can be applied to a lattice are:

- *Translation* **T** defined as

$$T = n_1\mathbf{a_1} + n_2\mathbf{a_2} + n_3\mathbf{a_3} \tag{2.3}$$

  is the operation that joins every couple of lattice points. A translation applied to all the points of the lattice results in the lattice itself.

- *Rotation* is a point symmetry operation. It consists of the rotation of the lattice of an angle ϕ around an axis passing through a lattice point, resulting in the lattice itself. To obtain a rotation of a plane lattice must be satisfied

$$|2a_1 cos\phi| = ma_1 \tag{2.4}$$

with m non-negative integer. The values of the angle ϕ that satisfy Eq.2.4 in order to obtain symmetry operations are

$$\phi = 2\pi/n \tag{2.5}$$

with $n = 1, 2, 3, 4, 6$ and are called $n-$fold rotation axes.

- *Mirror* **m** is the operation that maps the lattice into itself through a plane of reflection, and this plane passes through a lattice point (for this reason it is a point symmetry operation).

- *Inversion* occurs when a point is a center of symmetry of the lattice, i.e. by taking this point as the origin in a rectangular coordinate system, any point of coordinates (x, y, z) can be mapped in the opposite point $(-x, -y, -z)$ whithout altering the lattice.

- *Rotoinversion* is the combination of two point symmetry operations, a rotation and an inversion.

In three-dimensions it has been proven that all the crystals can be characterized by 32 point groups. These groups identify the 32 crystal systems, each one with its own symbol, that can be grouped in 7 crystal families or systems. By combining all the 32 point groups with translation it is possible to get 230 different spatial groups, that can be described by the means of geometric algebra [7].

2.4 Bravais lattices

In three-dimensions, a unit cell can be described with the vectors **a**, **b** and **c** and the angles α between **b** and **c**, β between **a** and **c**, and γ between **a** and **b** as can be seen in Fig. 2.1 . The vectors **a**, **b** and **c** identify the directions of the cell and are called crystallographic axes. They can be different from a cartesian coordinate system. The length of the vectors, a, b and c and the values of the angles α, β and γ are the *lattice parameters*. The relations among them allow the definition of 14 different *Bravais lattices.*
Due to symmetry characteristics, the 14 Bravais lattices can be grouped in 7 lattice systems with different lattice centering. In Tab. 2.1 can be seen the 7 lattice systems. The unit cell can be of different types:

- **P**, is the primitive or simple unit cell, with lattice points only on the corners of the cell,

- **I**, is the body centered cell, with lattice points on the corners and on the center of the cell

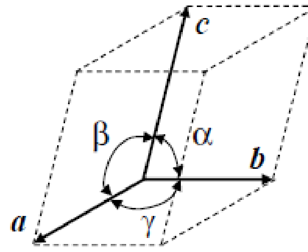

Figure 2.1: Directions and angles of a generic lattice unit cell [6]

System	Lattice parameters	Unit cell
Triclinic	$a \neq b \neq c$ $\alpha \neq \beta \neq \gamma \neq \pi/2$	Primitive (P)
Monoclinic	$a \neq\neq c$ $\alpha = \beta = \pi/2 \neq \beta$	Primitive (P) Base centered $A/B/C$ (A/B/C)
orthorhombic	$a \neq b \neq c$ $\alpha = \beta = \gamma = \pi/2$	Primitive (P) Bace centered A/B/C (A/B/C) Body centered (I) Face centered (F)
Tetragonal	$a = b \neq c$ $\alpha = \beta = \gamma = \pi/2$	Primitive (P) Body centered (I)
Hexagonal	$a = b \neq c$ $\alpha = \beta = \pi/2, \gamma = 2\pi/3$	Primitive (P)
Rhombohedral	$a = b = c$ $\alpha = \beta = \gamma \neq \pi/2$	Primitive (P)
Cubic	$a = b = c$ $\alpha = \beta = \gamma = \pi/2$	Primitive (P) Body centered (I) Face centered (F)

Table 2.1: The lattice systems

- **F**, is the face centered cell, with lattice points on the corners and at the center of each face of the cell
- **A/B/C**, is the base centered cell, with lattice points on the corners and at the center of each face of two parallel faces. The letter used to define this unit cell is the direction along the edge of the cell that connects the additional points at the center of the faces.

The 7 lattice systems are slightly different from the crystal systems, as can be seen in Tab. 2.2.

2.5 Miller indices

It is very useful to have a simple notation to describe the planes and the crystal directions of the crystal lattice.

Crystal system	Point groups #	Lattice system
Triclinic	#2	Triclinic
Monoclinic	#3	Monoclinic
Orthorhombic	#3	Orthorhombic
Tetragonal	#7	Tetragonal
Hexagonal	#7	Hexagonal
Trigonal	#5	Rhombohedral Hexagonal
Cubic	#5	Cubic
	Total#: 32	

Table 2.2: Point groups in three dimensions

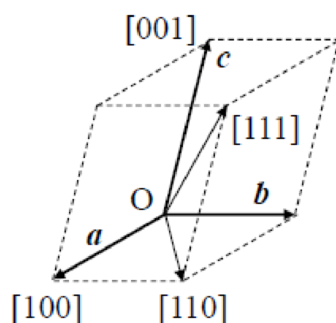

Figure 2.2: Coordinates of lattice points [6]

Each point of the lattice can be denoted with its own coordinates in a coordinate system conveniently chosen, e.g. a coordinate system whose axes are along the edges of the unit cell and with the unit distance equal to the dimensions of the unit cell, as can be seen in Fig. 2.2. Let us take a coordinate system and a plane that intercepts the axes at distances from the origin respectively of u, v and w. Let us take the reciprocals of u, v and w and multiply the three reciprocals by their least common denominator, in order to obtain three integers. The obtained three values are indicated as h, k and l and are the Miller indices, with the notation (hlk). Some examples of the Miller indices of some planes can be seen in Fig. 2.3. By taking a line passing through two lattice point it is possible to define this line with the vector that links that two points, i.e. with the indices of the direction, which are used to define the whole family of parallel lines to the one considered. The three components of the direction are written between square brakets, to avoid

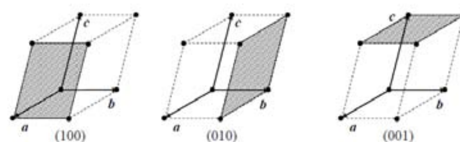

Figure 2.3: Examples of Miller planes [6]

mistakes with the round brackets of the plane indices.
The negative components of a vector or of a plane are written with a bar above the corresponding digit, e.g. the plane that intercepts the axes in 2, 1 and −1 can be written as $(12\overline{2}$ and the direction of the vector with components $-3, 1, 0$ is defined as $[\overline{1}30]$ [8].

Chapter 3

Piezoelectricity

3.1 Introduction

Piezoelectricity is the property of some classes of crystals to generate a potential difference when subject to a mechanical deformation, showing a *direct piezoelectric effect* and to deform elastically when subject to an electric field, in the *converse piezoelectric effect*, showing that this is a reversible process. The meaning of the name is *electricity from pressure* and it has been observed for the first time on Rochelle's Salt, whose first recorded synthesis was on 1655. The first systematic studies has been done by Curie brothers in 1880. In their work they established the existence of the direct piezoelectric effect and identified Rochelle Salt and other crystals, like quartz and tourmaline as piezoelectric crystals, by measuring the surface charge of these crystals [9].
The existance of the converse piezoelectric effect has been initially deduced by Lippmann and subsequently measured by the Curie brothers.
The first real application of the piezoelectricity has been developed as a response to the urgent demand of submarine warfare during World War I, and resulted in the first underwater source of sound, the sonar, with quartz element between steel sheets. This led to the most important research program on piezoelectricity in the U.S., directed by Walter Cady [10].
The majority of the most widely diffused applications of piezoelectric materials, like microphones, ultrasonic transducers, accelerometers, phonograph pick-ups and filters, has been firstly made between WWI and WWII. The effectiveness of these application was limited by the small piezoelectric properties of these materials, which were mainly single crystals. The discovery of the piezoelectric effect shown by some metal oxides, which were sintered under a strong electric field, brought a new class of materials to study: the piezoceramic materials.
The research on piezoceramics led initially to the realization of a piezoelectric ceramic based on barium titanate $BaTiO_3$ and later on the development of lead zirconate titanate, PZT, that is a solid solution of $PbTiO_3$ at $52-54\%$ and $PbZrO_3$ at $48-46\%$. This solid solution system is also denoted as $Pb(Ti,Zr)O_3$. The crystal structure of PZT is called *perovskite* and shows a non-symmetric tetragonal unit cell until the Curie temperature T_c, which is between 220 and $350°C$. Above this temperature the structure becomes symmetric and cubic.

The existance of an abrupt transition from the rhombohedrical to the tetragonal structure when the composition is near $PbZrO_3 : PbTiO_3 = 1 : 1$ shows a peak of the permittivity, which is used in commercial application of PZT.
This material, PZT is quite easy to realize in a laboratory, from the sintering of perovskitic powders, since it follows the typical process of production of ceramic materials.
The best performance are obtained with a composition almost stoichiometric, with a small amount of impurities and the highest density. Therefore, to limit the contamination during the mixting, are used zirconia grinding media.
The major problem during the sintering, that occurs at around $1300°C$, is the loss of lead, which is higly volatile above $800°C$. The solution of this problem is the sintering into an allumina vessell with a large quantity of lead-containig powder, such as $PbZrO_3$. In the sintered pieces are applied silver containing electrodes, which are used for the *poling* process, i.e. the application of a strong constant electric field $(1 - 4MV/m)$ at $100 - 150°C$.

3.2 Piezoelectric Effect

The piezoelectric effect, analyzed by the Curie brothers can be distinguished in *direct* and *indirect*. The direct piezoelectric effect represents the polarization of some charges on the surface of the material, after the application of a mechanical stress, while the converse piezoelectric effect is related to the deformation of the material as a consequence of the application of an electric field.
Piezoelectric materials are also dielectric materials. Inside it can be present permanent electric dipoles. The polarization of a dielectric material occurs when an electric field is applied externally, inducing the *polarization* of the material.
The polarization is a vector field that expresses the density of electric dipole moments, which can be permanent or induced, in a dielectric material. The application of an external electric field to a dielectric make its molecules gain electric dipole moment and the dielectric becomes polarized. The electric dipole moment induced per unit volume of the dielectric material is called the electric polarization of the dielectric [11]. The relation electric field and electric displacement field with the polarization can be written, for an isotropic material, as

$$\mathbf{D} = \varepsilon_0 \mathbf{E} + \mathbf{P} \tag{3.1}$$

where $\mathbf{E}$ is the electric field, $\mathbf{D}$ is the electric displacement field and ε_0 is the electric permittivity of vacuum, $\varepsilon_0 = 8.854 \times 10^{-12} C^2/(Nm^2)$.
The polarization is null outside the dielectric material, while the electric field is present also outside the dielectric.
For an anisotropic material, the permittivity and the dielectric susceptibility are second-rank tensor related as

$$[\varepsilon_r] = [I] + [\chi] = (1/\varepsilon_0)[\varepsilon] \tag{3.2}$$

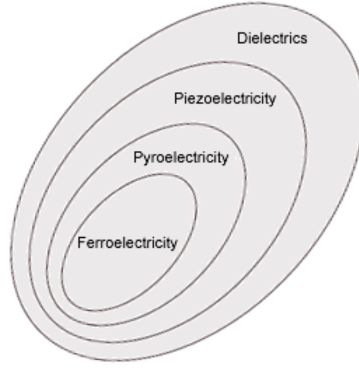

Figure 3.1: Dielectric, Piezoelectric, Pyroelectric and Ferroelectric Materials [13]

therefore the Eq. 3.1 for an anisotropic material can be written as

$$\begin{bmatrix} D_x \\ D_y \\ D_z \end{bmatrix} = \varepsilon_0 \begin{bmatrix} 1 & 0 & 0 \\ 0 & 1 & 0 \\ 0 & 0 & 1 \end{bmatrix} \begin{bmatrix} E_x \\ E_y \\ E_z \end{bmatrix} + \varepsilon_0 \begin{bmatrix} \chi_{11} & \chi_{12} & \chi_{13} \\ \chi_{21} & \chi_{22} & \chi_{23} \\ \chi_{31} & \chi_{32} & \chi_{33} \end{bmatrix} \begin{bmatrix} E_x \\ E_y \\ E_z \end{bmatrix} \tag{3.3}$$

which is also equal to

$$\begin{bmatrix} D_x \\ D_y \\ D_z \end{bmatrix} = \varepsilon_0([I] + [\chi]) \begin{bmatrix} E_x \\ E_y \\ E_z \end{bmatrix} = \varepsilon_0[\varepsilon_r] \begin{bmatrix} E_x \\ E_y \\ E_z \end{bmatrix} = [\varepsilon] \begin{bmatrix} E_x \\ E_y \\ E_z \end{bmatrix} \tag{3.4}$$

The axes x, y and z are arbitrary, therefore the tensors $[\chi]$, $[\varepsilon_r]$ and $[\varepsilon]$ can be written with respect to their principal axes, and their values must satisfy Neumann's principle. This principle, or principle of symmetry, states that, if a crystal is invariant with respect to certain symmetry operations, any of its physical properties must also be invariant with respect to the same symmetry operations, or otherwise stated, the symmetry operations of any physical property of a crystal must include the symmetry operations of the point group of the crystal [12].
The three main mechanisms of polarization of dielectric materials are electronic, ionic and dipolar orientation. Piezoelectric materials, which are a subset of dielectric materials, can be polarized in a different way, i.e. with the application of a mechanical stress.
Among the 32 crystal classes, 21 are non-centrosymmetric, in particular there are 11 non-polar and 10 polar. 20 of the 21 non-centrosymmetric classes, are piezoelectric materials, the only exception is a non-polar class.
The 10 polar classes of piezoelectric materials, have another important property, called *pyroelectricity*, i.e. they show a variation of polarization by varying the temperature.
Some pyroelectric crystals are also *ferroelectric* crystals (Fig. 3.1), i.e. they have a spontaneous electric polarization that can be reversed by the application of an external electric field, showing an hysteresis loop [6].

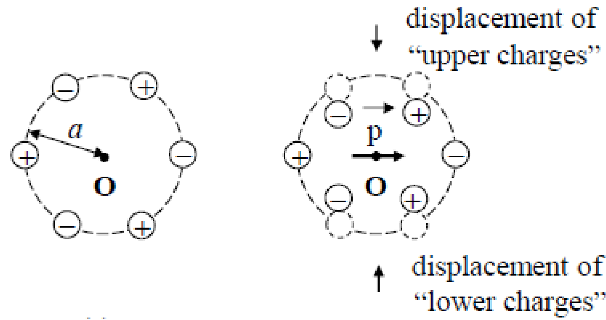

Figure 3.2: Dipole moment as a consequence of the displacement of charges

3.2.1 Direct Piezoelectric Effect

The displacement vector between two charges of equal magnitude but opposite sign, at very small distance a is directed from the negative to the positive charge. The dipole moment in this case is

$$\mathbf{p} = q\mathbf{a} \tag{3.5}$$

Given a small volume ΔV, the electric moment per unit volume is the ratio between the sum of all the dipole moments inside ΔV and ΔV itself is the polarization $\mathbf{P}$

$$\mathbf{P} = \frac{\sum_n \mathbf{P_n}}{\Delta V} = \frac{\Delta \mathbf{p}}{\Delta V} \tag{3.6}$$

By taking three charges placed at the corners of an equilateral triangle, and other three charges of the opposite sign at the corners of another equilateral triangle of the same size, and the same center, rotated of $\pi/3$, the centroid of the positive and the negative charges are overlapped.
The application of a mechanical force results in a displacement of the charges, which causes a non-null dipole moment, as can be seen in Fig. 3.2.
By repeating this analysis on the whole volume of the piezoelectric material, and by placing two electrodes at the two ends, it is possible to assume the presence of a uniform polarization. The result is a polarization surface charge equivalent to the uniform polarization.
The application of a mechanical stress on the piezoelectric material, e.g. with the application of a compression force, results in the strain of the body and in an equivalent polarization surface charge.
This effect, in a simple case, can be written as a direct proportionality of the stress σ with the polarization P

$$P = d\sigma \tag{3.7}$$

where the d is the piezoelectric constant of the material.
The analysis of the simple case can be adjusted to a three-dimensional model with the use of tensor theory.
The first thing to use, to simplify the study, is the symmetry of the stress tensor, due to energetic considerations; in this way it is possible to reduce the second rank

tensor as a single column of six elements. Therefore, since the polarization is a vector, the piezoelectric constants can be reduced to 18:

$$\begin{bmatrix} P_1 \\ P_2 \\ P_3 \end{bmatrix} = \begin{bmatrix} d_{11} & d_{12} & d_{13} & d_{14} & d_{15} & d_{16} \\ d_{21} & d_{22} & d_{23} & d_{24} & d_{25} & d_{26} \\ d_{31} & d_{32} & d_{33} & d_{34} & d_{35} & d_{36} \end{bmatrix} \begin{bmatrix} \sigma_1 \\ \sigma_2 \\ \sigma_3 \\ \sigma_4 \\ \sigma_5 \\ \sigma_6 \end{bmatrix} \tag{3.8}$$

3.2.2 Converse Piezoelectric Effect

The converse piezoelectric effect explains the mechanical deformation of a piezoelectric material as a consequence of the application of an electric field. The linear model that explains this effect has the same constant of proportionality of the direct effect d

$$\varepsilon = dE \tag{3.9}$$

In full form the Eq 3.9 becomes, since also the strain matrix is symmetric and can be simplified in a six element column

$$\begin{bmatrix} \varepsilon_1 \\ \varepsilon_2 \\ \varepsilon_3 \\ \varepsilon_4 \\ \varepsilon_5 \\ \varepsilon_6 \end{bmatrix} = \begin{bmatrix} d_{11} & d_{21} & d_{31} \\ d_{12} & d_{22} & d_{32} \\ d_{13} & d_{23} & d_{33} \\ d_{14} & d_{24} & d_{34} \\ d_{15} & d_{25} & d_{35} \\ d_{16} & d_{26} & d_{36} \end{bmatrix} \begin{bmatrix} E_1 \\ E_2 \\ E_3 \end{bmatrix} = [d]^T \begin{bmatrix} E_1 \\ E_2 \\ E_3 \end{bmatrix} \tag{3.10}$$

Supposing a linear relation between the stress $[\sigma]$ and the strain $[\varepsilon]$, with tensor notation, results

$$[\sigma] = [c][\varepsilon] \tag{3.11}$$

or

$$[\varepsilon] = [s][\sigma] \tag{3.12}$$

where $[c]$ is the stiffness matrix and $[s]$ is the compliance matrix, which are $6x6$ tensors, with

$$[c] = [s]^{-1} \tag{3.13}$$

and viceversa. Both the matrices are symmetric, due to energetic considerations, so the number of indipendent values are 21 instead of 36.

3.2.3 Linear Piezoelectric Material

At constant temperature, both the strain and the displacement are dependent from the stress and the electric field, due to direct and converse piezoelectric

effect. Working with small variations from a set point, it is possible to write for a simple system

$$\begin{cases} \Delta\varepsilon = \frac{\partial\varepsilon}{\partial\sigma}\Delta\sigma + \frac{\partial\varepsilon}{\partial E}\Delta E \\ \Delta D = \frac{\partial D}{\partial\sigma}\Delta\sigma + \frac{\partial D}{\partial E}\Delta E \end{cases} \tag{3.14}$$

Some considerations that can be applied to Eq. 3.14 are that from thermodynamics and energy considerations, the partial derivatives to be identified are only three, since

$$\frac{\partial\varepsilon}{\partial E} = \frac{\partial D}{\partial\sigma} = d \tag{3.15}$$

The other two partial derivatives are the compliance and the permittivity, which are calculated at constant electric field, indicated with superscript E.

$$s^E = \frac{\Delta\varepsilon}{\Delta\sigma}|_{\Delta E=0} \quad = \frac{\Delta\varepsilon}{\Delta\sigma}|_{E=const} \tag{3.16}$$

and

$$\varepsilon_0\varepsilon_r^\sigma = \frac{\Delta D}{\Delta E}|_{\Delta\sigma=0} \quad = \frac{\Delta D}{\Delta E}|_{\sigma=const} \tag{3.17}$$

In this way Eqs. 3.14 become

$$\begin{cases} \varepsilon = s^E\sigma + dE \\ D = d\sigma + \varepsilon_0\varepsilon_r E \end{cases} \tag{3.18}$$

The equations are easy to write in tensor notation:

$$\begin{cases} [\varepsilon] = [s^E][\sigma] + [d]^T[E] \\ [D] = [d][\sigma] + \varepsilon_0[\varepsilon_r^\sigma]\,[E] \end{cases} \tag{3.19}$$

Piezoelectric Directions

The piezoelectric effect as can be seen in Eq. 3.19 act adding a term both to the Hooke's law and to the electric displacement field.
The tensor relations can be split and analysed depending on the directions considered.
There are different ways to convert mechanical energy into electrical energy through a piezoelectric material:

- 33 effect, with a transverse solicitation, both the stress and the polarization are along the direction 3.
- 31 where the solicitations is along the longitudinal direction 1 and the polarization occurs along direction 3.
- 14 is the harvesting of electrical energy along direction 1 as a consequence of a shear stress defined as direction 4.

Property	Value
Chemical Formula	AlN
Density	$3.26g/cm^3$
Molecular mass	$40.9882g/mol$
Melting point	$2472°C$
Boiling point	$2517°C$
Band gap	$6.015eV$
Electron mobility	$300cm^2/Vs$
Thermal conductivity	$285W/mK$
Refractive index	$1.9 - 2.2$
Space Group	$P6_3mc$

Table 3.1: Properties of AlN

3.3 Aluminum Nitride

The piezoelectric material used in this work is aluminum nitride. It has been chosen since it is a lead-free piezoelectric material and furthermore it is easy to deposite as thin film with magnetron sputtering.
AlN is a nitride of aluminum, with a wurztite structure that is also written as $w - AlN$ and it was first synthesized in 1877.

3.3.1 Properties of Aluminum Nitride

The wurztite phase of AlN with a band gap of $6.01 - 6.05eV$ is one of the wide band gap semiconductors. In Tab. 3.1 there are some of the properties of the AlN

The bonding energy of the atoms of the aluminum nitride is high, implying a high hardness of the material, a high melting point and a high Young's modulus. This property is highly directional, due to covalent bonds.
The wurtzitic phase is a non-centrosymmetric structure, with an hexagonal crystal lattice (Fig. 3.3). The lattice constant are

- $a = 3.111Å$
- $c = 4.979Å$

with a hexagonal structure and $P6_3mc$ space group [14].
In the crystal structure, the Al atom constitute the hexagonal structure while the nitrogen atom occupy the half of the tetrahedrical positions of the structure, as can be seen in Fig. 3.4.

3.3.2 Piezoelectric Properties of Aluminum Nitride

In the work of Prof. Muralt and M.A. Dubois [15] has been collected some values of piezoelectric coefficient d_{33_f} of $w - AlN$ reported in literature, where the

Figure 3.3: Hexagonal crystal lattice

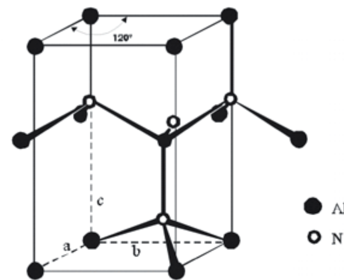

Figure 3.4: Structure of AlN

subscript f stands for *film*, meaning that the aluminum nitride is clamped on a rigid substrate. The magnitude of this value varies from $1.6pm/V$ to $5.56pm/V$ according to the substrate and the growth method.
For pulsed dc sputtering the values found in the same work are in magnitude of $d_{33_f} = 3.4pm/V$ and $3.9pm/V$.
In that work, has been analyzed also the variation of d_{33_f} by varying the process parameters. The result showed a great variability of the piezoelectric coefficient. Another important result is the variation of internal stress, which affect also the piezoelectric constant, with the variation of process parameters.

3.3.3 Synthesis of Aluminum Nitride

There are different ways to syntesize aluminum nitride, e.g. from carbothermal nitridation reaction, which can be used to synthesize cubic aluminum nitride [16]. In this work the synthesis of AlN is done from direct reaction of aluminum with nitrogen:

$$2Al + N_2 \rightarrow 2AlN \tag{3.20}$$

Chapter 4

Thin Film Deposition Techniques

Thin films are defined as layers of material ranging from the nanometric scale to several micrometers in thickness which are deposited on the surface of another material, called substrate.
The starting material is called *target* and can be metallic, semiconductive or insulating.
The thin film deposition techniques can be grouped in three main categories:

- deposition from *solid phase*, e.g. solid phase precipitation
- deposition from *liquid phase*, e.g. metal plating
- deposition from *gaseous phase* or *vapor*

Another way to group the deposition techniques is by type of process, which can be *physical* or *chemical* (Fig.4.1).
The gaseous-phase techniques can be divided therefore in

- chemical vapor deposition, *CVD*
- physical vapor deposition, *PVD*

4.1 Chemical Vapor Deposition

The chemical vapor deposition processes are

- thermal CVD
- plasma enhanced CVD
- laser assisted CVD

These processes are based on a series of consecutive chemical reactions. This allow to obtain a deposition of a material, which is introduced in the reaction chamber in gaseous state and reacts, decomposing on the surface of the substrate.
The substrate is typically exposed to one or more precursors. Into the reaction chamber they react or decompose on the substrate surface, producing the thin film

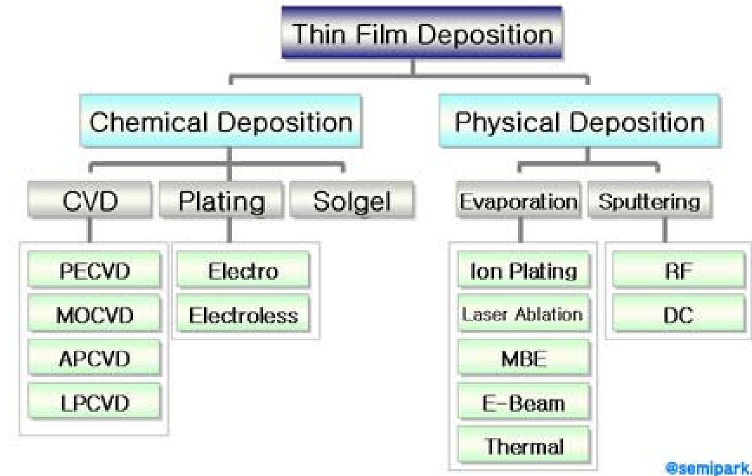

Figure 4.1: Thin film deposition categories [17]

deposite.
CVD processes can be practiced in many ways, e.g. at atmospheric pressure, at low-pressure or in ultrahigh vacuum, with reactions enhanced by plasma or by laser. CVD is also one of the most effective ways to obtain extremely thin layers. The other main advantages are

- good density and homogeneity even on rough surfaces
- high purity of the deposit
- simple and cheap process

The disadvantages instead are

- high quality precursors
- complex and expensive control systems
- high temperature of the substrate
- low deposition rates

4.2 Physical Vapor Deposition

In CVD the material to be deposited becomes a part of the substrate, by reacting with it while with the physical vapor deposition the process molecules remain separate from the substrate even if they form a single and homogeneous body.
The evaporation of the material to be deposited can be done in different ways, like

- thermal PVD, which is the simplest method. The metallic vessel containing the target is heated by the high current density. This causes the evaporation of the target. The vapor then reaches the surface of the substrate, creating a thin film

- electron beam PVD. This technique is based on the heating of the target by an electron beam. The electron beam is created by a wire that produces an electric current while heated. The current is then directed to the target by a magnetic field

- arc-PVD or cathodic arc deposition. The arc discharge formed between the target and the electrode causes the ionization of the process gas, ionizing it. This plasma causes the ions to hit the target. The particles undermined by the impacts can arrive directly on the substrate, depositing on it.

4.2.1 Magnetron Sputtering

The laboratory of Micro and Nanostructured Materials of the Industrial Engineering Department has a magnetron sputter with an unbalanced configuration.
The sputtering technique is a physical vapor deposition technique that can be performed by direct current,

Phenomena Involved in a Plasma

The gas present in a PVD chamber is characterized by some parameters. The atoms of the gas have a mean velocity that is a function of the absolute temperature

$$\bar{c} = \left(\frac{8k_bT}{\pi m}\right)^{1/2} \tag{4.1}$$

where $k_b = 1.3806488 \times 10^{-23} J/K$ is the Boltzmann constant, T is the absolute temperature in K and m is the mass of the particle. Due to random collisions between the particles, the individual velocity of the particles can be described with a Maxwell-Boltzmann distribution function, i.e. nearly 90% of the particles have a velocity between $\frac{1}{2}\bar{c}$ and $2\bar{c}$. The pressure into the chamber is defined by the number of hits of the particles on the walls of the chamber itself, and depends on the density of gas atoms n, on the mass m and the mean square velocity $\bar{c}^2$

$$p = \frac{nm\bar{c}^2}{3} = nk_bT \tag{4.2}$$

Furthermore, the pressure can be adjusted by varying the flux of gas that enters into the chamber, to maintain a specific operating pressure.
Another important parameter of a ionized gas is the degree of ionization α defined as

$$\alpha = \frac{n_i}{n_i + n_0} \tag{4.3}$$

By calling $2a_i$ the diameter of the incident particle and $2a_n$ the diameter of a generic particle, the collision cross section is

$$\sigma_c = \pi(a_i + a_n)^2 \tag{4.4}$$

The flux of particles i is therefore reduced by the collisions with the particles n. The reduction of flux Γ_i after traversing the slab of n particles is, after a distance x,

$$\Gamma_i = \Gamma_0 e^{-\frac{x}{\lambda}} \tag{4.5}$$

where λ is the mean free path for collision, calculated as

$$\lambda = \frac{1}{n_n \sigma_c} \tag{4.6}$$

with n_n the number of n particles.
The collision frequency of particle with velocity v_i can be easily calculated as

$$\nu_c = \tau^{-1} = \frac{v_i}{\lambda} = n_n \sigma_c v_i \tag{4.7}$$

which can be averaged over the distribution function

$$\nu_c = n_n \langle \sigma_c v_i \rangle \tag{4.8}$$

Since the coulomb force is a long-range force the deflection of the trajectory of electrons colliding with ions starts at far distance, conversely from electrons that collide with neutrals.
The frequency of collision can be calculated from the Coulomb force and results

$$\nu_c = \frac{ne^4}{16\pi\varepsilon_0^2\sqrt{m_e}(k_b T_e)^{\frac{3}{2}}} \tag{4.9}$$

By considering that the cumulative effect of small-angle collisions is larger than the effect of large-angle, Eq.4.9 can be multiplied by the coulomb logarithm $ln(\Lambda)$ and divided by $\pi^{\frac{1}{2}}$, resulting in

$$\nu_c = \frac{ne^4 ln(\Lambda)}{16\varepsilon_0^2\sqrt{m_e}(\pi k_b T_e)^{\frac{3}{2}}} \tag{4.10}$$

Considering the main collisional processes, there must be an external source of energy to maintain ionization and to balance the relaxation processes. Since the mass of the electron is much smaller than the mass of the ions, the electric field gives energy primarily to the electrons. Therefore electrons can have a high average kinetic energy while the ions can remain essentially at room temperature. The temperature of the electrons is therefore related to the kinetic energy:

$$\frac{1}{2} m_e \overline{c_e}^2 = \frac{3}{2} k_b T_e \tag{4.11}$$

[18, 19].

Magnetron Sputtering Process

The films that can be obtained are produced by sputtering the target surface with plasma ions with high kinetic energy. These ions impact with the target, resulting in the ejection of species from the target. This particles are called adatoms and can be deposited directly on the substrate or can react with a gas that can be present in the plasma before depositing on the substrate.
An important parameter for the sputtering process is the sputtering yeld, S which is the ratio between the adatoms emitted by the target. The sputtering yeld is related to

- the trajectory of the plasma ions
- the kinetic energy of the impacting ions, i.e. their mass and velocity
- the crystal structure of the target
- the process gas

The most used sputtering processes have a sputtering yeld between 0.1 and 10.
The effect of the mass, the kinetic energy and the trajectory can be described by

$$\frac{E_t}{E_i} = \frac{4m_t m_i cos^2\theta}{(m_t + m_i)^2} \tag{4.12}$$

where E_t is the kinetic energy of the target particle, E_i is the kinetic energy of the incident particle, m_t is the mass of the target particle,m_i is the mass of the incident particle and θ is the angle of the trajectory of the incident particle with respect to the target surface.
The magnetron sputtering is a variation of the sputtering technique, used to increase the path of the electrons to the anode.
To obtain this result it is used the *magnetic mirror* configuration. In this way the electrons undergo to the Lorentz force, that is perpendicular to **B**

$$\mathbf{F} = q\mathbf{v} \times \mathbf{B} \tag{4.13}$$

where q is the charge of the particle, **v** its velocity and **B** the magnetic field.
The Lorentz force does not provide work to the particle, but exerts a centripetal force, with Larmor radius r_L,

$$r_L = \frac{mv_\perp}{qB} \tag{4.14}$$

and cyclotron frequency ω_c

$$\omega_c = \frac{v_\perp}{r_L} = \frac{qB}{m} \tag{4.15}$$

In this case, the magnetic mirror configuration is created by placing permanent magnets under the target, as can be seen in Fig. 4.2. The Lorentz force tends to maintain the electrons in the zone with low values of **B**, i.e. near the surface of the target.
In this way the collision frequency is increased, therefore there is a higher number

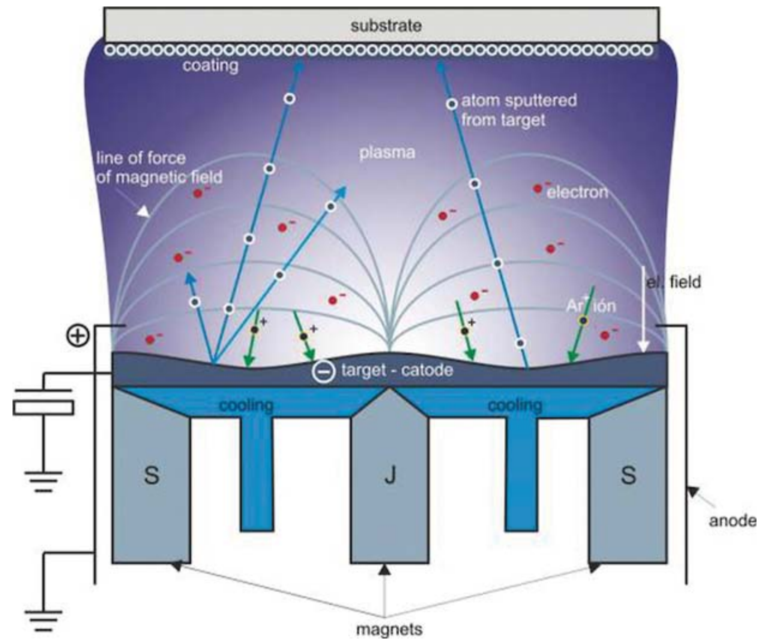

Figure 4.2: Magnetron sputtering, sputtering with magnetic mirror configuration [20]

of ions of the plasma that hit the target.
The magnets used to create the magnetic mirror configuration are permanent magnets, therefore they must operate far below their Curie temperature. The power of the discharge led to the increase of the temperature of the cathode and the magnets, which is maintained constant with an external cooling system.
The current density J on the target is not constant due to the presence of the magnets and the magnetic mirror configuration. This led to a different erosion rate of the target, as can be seen in Fig. 4.3. The magnetic field that can be obtained in the magnetron configuration can be classified in three types

- balanced field configuration
- unbalanced field configuration
- mixed field configuration

The balanced configuration (Fig. 4.2, a) has the flux of the magnetic field induction **B** that goes through the central magnet, completely closed on the external magnets. In this configuration the plasma is strongly confined in the region near the target. The negative effect is the low ionic current towards the substrate, which could be increased with the application of a negative potential to the substrate, which is difficultly feasible.
The unbalanced configuration has a less effective confinement of the electrons. In this way it is possible to increase the density of the plasma also in the zone near the substrate, increasing the effectiveness of the deposition.
The unbalanced configuration has two types, the first one (Fig. 4.2, b) has a flux of magnetic induction field greater on the central magnet than on the external

Figure 4.3: Aluminum (99.9999%) target used in the magnetron sputter of the laboratory of Micro and Nanostructured Materials

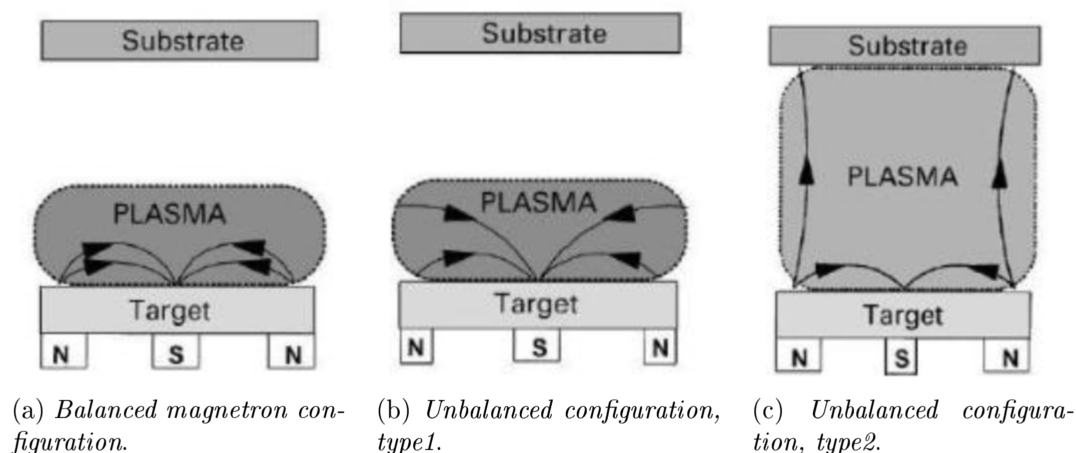

(a) *Balanced magnetron configuration.* (b) *Unbalanced configuration, type1.* (c) *Unbalanced configuration, type2.*

Figure 4.4: Magnetron sputtering configurations [21]

magnets. The magnetic field lines are partially closed on the external magnets, while the rest are closed passing through the walls of the chamber. This configuration increases the deposition rates of substrates which are not perfectly facing the target.
The second type (Fig. 4.2, c) has a flux of magnetic induction field stronger on the external magnets. The magnetic field lines therefore closes partially on the central magnet and partially not, passing through the substrate, increasing the plasma density on it, without the need of polarizating it.
The mixed configuration uses a multiple magnetron configuration.

4.3 Thin Film Formation

The particles that impact on the substrate are mainly in atomic or in molecular form. An atom migrates on the surface of the substrate to join other migrating atoms to form a more stable pair or it evaporates. The motion of the atom is determined by its binding energy with the substrate and the effect is the hopping of the atom from an adsorption site to another. The probability of forming an atomic pair is related to the density of the single atoms and the deposition rate. The doublets atc as nucleation sites, leading to the formation of quasi-stable islands. After the nucleation stage, the growth rate overcomes the nucleation rate, and islands start to grow in size rather than in number, in the agglomeration stage. During this process, the film reaches continuity.
The formation of the film and the resulting structure is extremely sensitive to the process parameters. The flux and the energy of the charged particles that reaches the substrate can be adjusted by changing the electric field.

Chapter 5

Kinetic Energy Harvesting

The kinetic energy harvesting refers to techniques used by electric or electronic devices to collect and convert the energy of the surrounding enviroment. E.g. the kinetic energy that can be generated by the vibrations of a rotating motor, by a man running, etc.
These devices can typicaly generate a small power, which can be used to feed sensors or small circuits. This circuits otherwise would be fed by external batteries, whose operating life is restricted to several years; conversely the energy harvesting devices have a operating life which is related only on their failure or breakage.
The aim of this work is the analysis and the realization of a kinetic energy harvester, which is designed to convert mechanical energy, from external vibrations, into electrical energy. This kind of device can work both as a primary energy source or as a backup energy source, alongside another primary energy source.
A promising technology and configuration for the kinetic energy harvesting is the piezoelectric resonating generator, in the cantilever configuration.

5.1 Kinetic-to-Electrical Energy Conversion

The conversion of mechanical energy into electrical energy can be operated by three main types of converters, that are

- electromagnetic
- electrostatic
- piezoelectric

The electromagnetic conversion is based on the Faraday's law of induction, where the electromotive force $e(t)$ can be calculated as

$$e(t) = \frac{d\phi_B(z(t))}{dt} = \frac{d\phi_B}{dz} \cdot \frac{dz}{dt} \tag{5.1}$$

where ϕ_B is the magnetic flux through the coil.
The electrostatic converter requires an external feeding system and works as a

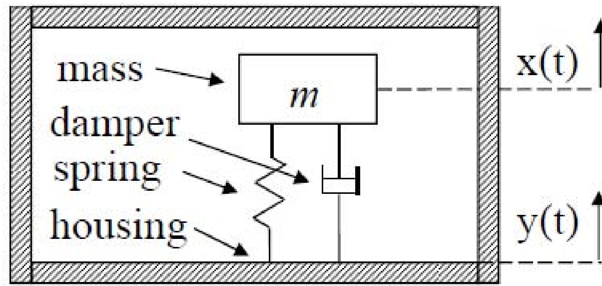

Figure 5.1: Mass spring damper system [6]

variable capacitor, with a fixed plate and a moving plate. This results in a variable capacitance. The stored energy in a capacitor is W_e with

$$W_e = \frac{1}{2}CV^2 = \frac{1}{2}QV = \frac{1}{2}\frac{Q^2}{C} \tag{5.2}$$

Since the distance between the two plates varies, the capacitance goes from a minimum capacitance, at the maximum distance, to a maximum value at the minimum distance. This results in a difference of the stored energy equal to ΔW_e

$$\Delta W_e = \frac{1}{2}Q^2\left(\frac{1}{C_{min}} - \frac{1}{C_{max}}\right) \tag{5.3}$$

The piezoelectric converter is based on a piezoelectric layer between two electrodes. The vibration of the converter causes a variation of the stress state of the material from tensile stress to compressive stress. Since the material is piezoelectric, this causes a variation of the potential difference between the electrodes, which are connected to the surfaces of that material.
The piezoelectric generator can be made with a single piezoelectric layer above a main substrate, in a *unimorph* configuration, or can be made by two piezoelectric layers, one above and one below the substrate, in a symmetric configuration called *bimorph*. In the bimorph configuration, when a layer undergoes a tensile stress, the other layer undergoes a compressive stress.

5.2 Electromechanical Model

The general model of electromechanical conversion, can be applied to all the three types of converters. This model is based on a *mass-spring-damper* system, as can be seen in Fig. 5.1. According to the notation of Fig. 5.1 the movement of the base is described by $y(t)$ while the movement of the mass is described by $x(t)$. The relative movement between the mass and the base is therefore $z(t)$, since the mass and the housing are not rigidly connected

$$z(t) = x(t) - y(t) \tag{5.4}$$

The forces that act on the mass are:

- inertial force $m\frac{d^2x(t)}{dt^2}$
- damping force $c\left(\frac{d}{dt}x(t) - \frac{d}{dt}y(t)\right)$
- force due to spring $k\left(x(t) - y(t)\right)$

Since the momentum of the system is constant, the sum of the forces is equal to 0. For this reason it is possible to write

$$m\frac{d^2x(t)}{dt^2} + c\left(\frac{d}{dt}x(t) - \frac{d}{dt}y(t)\right) + k\left(x(t) - y(t)\right) = 0 \tag{5.5}$$

Since $z(t) = x(t) - y(t)$ Eq. 5.5 can be written as

$$m\frac{d^2z(t)}{dt^2} + c\frac{dz(t)}{dt} + kz(t) = -m\frac{d^2y(t)}{dt^2} = F \tag{5.6}$$

The characteristic equation of the associated homogeneous differential equation is

$$\lambda^2 + \frac{c}{m}\lambda + \frac{k}{m} \tag{5.7}$$

The roots of Eq. 5.7 are

$$\lambda_{1,2} = -\frac{c}{2m} \pm \sqrt{\left(\frac{c}{2m}\right)^2 - \frac{k}{m}} \tag{5.8}$$

By introducing the natural frequency ω_n and the damping ratio ζ,

$$\omega_n = \sqrt{\tfrac{k}{m}}; \quad \zeta = \tfrac{c}{2m}\tfrac{1}{\omega_n} = \tfrac{c}{2\sqrt{mk}} \tag{5.9}$$

the roots, in Eq. 5.8, can be written as

$$\lambda_{1,2} = \left(-\zeta \pm \sqrt{\zeta^2 - 1}\right)\omega_n \tag{5.10}$$

Since the homogeneous differential equation tends to zero for every damping ratio greater than 0, can be neglected on the steady state study.
With a sinusoidal vibrating source, the movement of the base is

$$y(t) = Y_M sin(\omega t) = \sqrt{2}Y sin(\omega t) \tag{5.11}$$

and the resulting relative motion in sinusoidal steady state is

$$z(t) = Z_M sin(\omega t + \phi) = \sqrt{2}Z sin(\omega t + \phi) \tag{5.12}$$

By considering the sinusoidal functions Eq.s 5.11 and 5.12 as phasors

$$\overline{Y} = Ye^{j0}; \quad \overline{Z} = Ze^{j\phi} \tag{5.13}$$

the Eq.5.6 can be written as

$$|\overline{Z}| = \frac{1}{\sqrt{\left(1 - \left(\frac{\omega}{\omega_n}\right)^2\right)^2 + \left(2\zeta\frac{\omega}{\omega_n}\right)^2}}\left(\frac{\omega}{\omega_n}\right)^2 Y \tag{5.14}$$

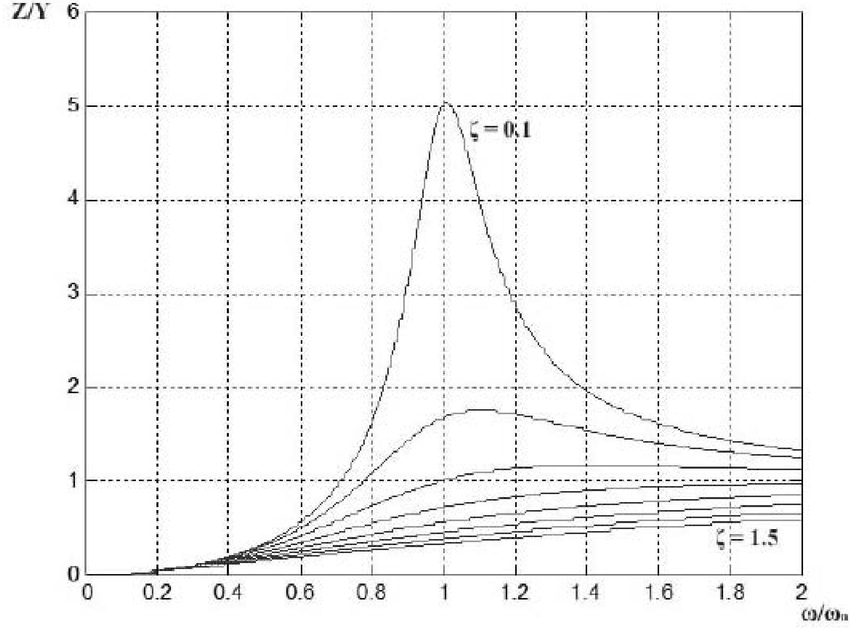

Figure 5.2: Behavior of the ratio of the amplitude of relative motion with the movement of the base, [21]

and

$$\angle\overline{Z} = \phi = -tan^{-1}\frac{2\zeta\frac{\omega}{\omega_n}}{1-\left(\frac{\omega}{\omega_n}\right)^2} \tag{5.15}$$

The behavior of the ratio of the amplitude of the relative motion with the movement of the base as a function of the damping ratio and of the frequency can be seen in Fig 5.2. To obtain the maximum movement of the cantilever, it should operate with a small damping ratio, near the frequency of resonance.
The electric power generated by the cantilever is related to the damping ratio, that is composed by a part which depends only on mechanical damping (with subscript m) and a part which depends on the energy conversion (with subscript e) so that c can be splitted as

$$c = c_m + c_e \tag{5.16}$$

into the Eq. 5.5.
The damping force results as

$$F_{damping} = (c_e + c_m)\frac{d}{dt}z(t) \tag{5.17}$$

while the relative velocity is

$$v_z(t) = \frac{d}{dt}z(t) \tag{5.18}$$

The power that can be extract results therefore as the product of the damping force multiplied by the relative velocity

$$p(t) = c\left(\frac{d}{dt}z(t)\right)^2 \tag{5.19}$$

With a sinusoidal source $\overline{Y}$ the power in sinusoidal steady state becomes

$$P = \frac{2\zeta m \left(\frac{\omega}{\omega_n}\right)^3 \omega^3}{\left(1 - \left(\frac{\omega}{\omega_n}\right)^2\right)^2 + \left(2\zeta \frac{\omega}{\omega_n}\right)^2} Y^2 \quad (5.20)$$

In the case of a sinusoidal source with a frequency equal to the resonance frequency, $\omega = \omega_n$, the power of Eq.5.20 becomes

$$P_{\omega=\omega_n} = \frac{m\omega_n^3}{4\zeta} Y_M^2 \quad (5.21)$$

The power related to the electrical energy is only a fraction of the total power. The converted power therefore can be calculated as

$$P_e = \frac{c_e}{c} P = \frac{\zeta_e}{\zeta} P = \frac{2\zeta_e m \left(\frac{\omega}{\omega_n}\right)^3 \omega^3}{\left(1 - \left(\frac{\omega}{\omega_n}\right)^2\right)^2 + \left(2\zeta \frac{\omega}{\omega_n}\right)^2} Y^2 \quad (5.22)$$

As in the case of the total power, with a frequency of the sinusoidal source equal to the resonance frequency, the electric power of Eq. 5.22 can be evaluated as

$$P_{e,\omega=\omega_n} = \frac{\zeta_e m\omega_n^3}{4\zeta^2} Y_M^2 = \frac{\zeta_e m\omega_n^3}{4(\zeta_e + \zeta_m)^2} Y_M^2 \quad (5.23)$$

In the Eq.5.23 can be seen that the electric power has a maximum for the mechanical damping ratio equal to the electrical damping ratio.

5.3 Cantilever Beam

The system that has been chosen in this work is the cantilever beam configuratin, with rectangular base.
The multilayer system, due to the reduced thickness of the layers on the substrate can be studied, in a first approximation, as made by only a single layer. By doing so, it is possible to study the eigenfrequency of the cantilever system, starting from the wave equation.
The application of a stress pulse to a homogeneous beam of constant section can be studied from the Hooke's law. The wave equation becomes

$$\frac{\partial^2 u(x,t)}{\partial t^2} = \frac{EAL}{m} \frac{\partial^2 u(x,t)}{\partial x^2} \quad (5.24)$$

where E is the Young's modulus, A is the cross section of the beam, L is the length and m is the mass. The equation 5.24 can be written as a function of the density ρ, becoming

$$\frac{\partial^2 u(x,t)}{\partial t^2} = \frac{E}{\rho} \frac{\partial^2 u(x,t)}{\partial x^2} \quad (5.25)$$

Since the constant of the wave equation is the square of the velocity, the speed of sound of a bar is

$$v_s = \sqrt{\frac{E}{\rho}} \tag{5.26}$$

The solution of the wave equation for the cantilever beam led to different modes of vibration, which are characterized by the roots of the following equation, where n refers to the $n-th$ mode of vibration

$$cos(C_n)cosh(C_n) = -1 \tag{5.27}$$

The most important in this analysis is the first mode, which is the simplest.
From the solution of the first mode, it is possible to calculate the resonance frequency of the cantilever f_1

$$f_1 = \frac{1}{2\pi}\frac{C_1^2}{L^2}\sqrt{\frac{EI}{\mu}} \tag{5.28}$$

where C_1 is the constant associated to the first mode and is $C_1 \simeq 1.875$, from Eq. 5.27, L is the length of the cantilever beam, E is the Young's modulus, I is the moment of inertia and μ is the mass per unit length. The equation 5.28 can be simplified by taking into account that the mass per unit length can be written as

$$\mu = \frac{m}{L} = \frac{A \times L \times \rho}{L} = A \times \rho \tag{5.29}$$

and the moment of inertia is equal to

$$I = \frac{wh^3}{12} \tag{5.30}$$

where w is the width of the cantilever and h is the heigth.
It results

$$f_1 = \frac{C_1^2}{2\pi\sqrt{12}}\frac{h}{L^2}\sqrt{\frac{E}{\rho}} \tag{5.31}$$

5.3.1 Effect of Deposition of Thin Film

The deposition of a thin film above the substrate changes the flexural rigidigy, influencing also the frequency of the beam's vibrations. The equations that led to the solution of the wave equation for the cantilever beam can be used also in this case, with some replacements. In particular the linear mass density of the cantilever beam becomes

$$\mu = \rho_s A_s + \rho_f A_f \tag{5.32}$$

where the subscript s stands for *substrate* and the subscript f stands for *film*.
Another important variation is the shift of the centroid and also a variation of the inertia

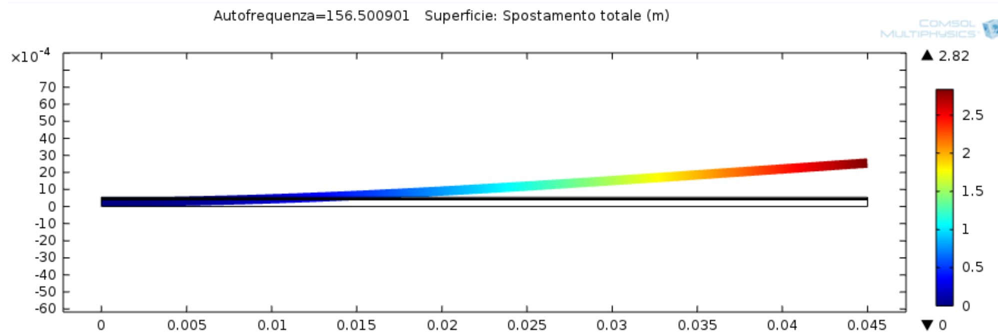

Figure 5.3: Result of the COMSOL multiphysics simulation for the FEM analysis of the resonance frequency of the cantilever

5.3.2 Comsol Multiphysics Analysis

By the means of the finite element method, has been implemented a simulation of the vibration of the whole system, composed by a copper substrate of $0.4mm$ thickness, a $2\mu m$ thick layer of aluminum nitride, a $66\mu m$ thick layer of polyimide and a $80\mu m$ thick layer of aluminum, with length $L = 45mm$. The resonance frequency calculated with COMSOL® for the composite structure is represented in Fig 5.3, and it is equal to $f = 156.5Hz$. By considering only the copper layer, with a Young's modulus of $E_{Cu} = 120GPa$ and a density of $\rho_{Cu} = 8920kg/m^3$, the resonance frequency from Eq. 5.31 is $f \simeq 117Hz$.

Chapter 6

Realization

The first step to realize a piezoelectric cantilever is the design of the layout.
The tipical commercial cantilever is made by a non-conductive and stiff substrate, with an electrode made by a thin film of conducting material, a piezoelectric layer and another layer of conducting material as top electrode.
In this work, the layout has been modified with a conductive and stiff substrate, a layer of aluminum nitride, a layer of polyimide tape and a layer of aluminum tape. In this way the polyimide layer ensures the electrical insulation between the upper electrode and the lower electrode also in the case of mechanical failure of the thin film of AlN; the possibility of short circuit between the upper and the lower electrode is avoided.
The second step is the choice of the material of the substrate. The available materials in the laboratory were aluminum, copper, brass and steel. The main requirement for the material of the substrate in this work were the thermal and the electrical conductivity. The choice has been restricted therefore to copper and aluminum.
The third step is the choice of the size of the substrate. In order to do so, it is necessary to chose an adequate resonance frequency that, for kinetic energy harvesting from vibrations, it is usually placed between $100Hz$ and $500Hz$ for commercial solutions. The available sheets in the laboratory were respectively 0.3, 0.8 and $1.5mm$ for the aluminum and 0.4 and $0.8mm$ for the copper.
Starting from Eq. 5.31 has been calculated a set of possible choices for the size of the cantilever. The first choice has been the $0.3mm$ thick aluminum sheet with a vibrating length of $45mm$, a total length of $70mm$ and a width of $15mm$. This choice has been made since the estimated frequency of this set of dimensions is $121.9Hz$, with a Young's modulus $E_{Al} = 70GPa$ and a density $\rho_{Al} = 2700kg/m^3$. This set of length and width has been maintained also for the other thickness and materials tested. In particular the second choice has been a $0.8mm$ thick aluminum sheet and the third has been a $0.4mm$ thick copper sheet.
For copper the Young's modulus is $E_{Cu} = 120GPa$ and the density is $\rho_{Cu} = 8920kg/m^3$. With $0.4mm$ thickness, it results a frequency of about $117Hz$.

Figure 6.1: Magnetron sputtering system of the laboratory of Micro and Nanostructured Materials of the University of Padua

6.1 Thin Film Deposition Equipment

The deposition of aluminum nitride and aluminum used in this work has been done with the magnetron sputtering system of the Micro and Nanostructured Materials Laboratory of the University of Padua (Fig. 6.1). This magnetron works in the unbalanced configuration of type 2 (Fig.4.4,c)[22].

The structure of the magnetron is made of stainless steel and the chamber, with a square base, has length and width of 457mm and heigth of 612mm. The steel door is surrounded by a Viton® seal and does not have any closing mechanism; it is large as the entire side of the chamber, to obtain an easy access and maintenance of the chamber. The door is kept closed by the pressure difference between air of the laboratory and inside the vacuum chamber.

At the inside, there are two disks, which are placed above the electrodes. Their diameter is of 440mm and they can be rotated from the outside, with a completely sealed mechanisms that allow the operations in vacuum. The lower disk is the shutter, which has two holes of 155mm of diameter, which are separated by an angle of 105° between their centers, as can be seen in Fig. 6.2,a. The external mechanism allow the rotation of the shutter in order to let four operating positions of the electrodes (Fig. 6.2,b):

- electrode 1 open, electrode 2 closed
- electrode 1 closed, electrode 2 open
- electrode 1 open, electrode 2 open
- electrode 1 closed, electrode 2 closed

The upper disk is used to hold the substrate and to position it above the electrodes, with an external mechanism. Its height can be set at different discrete values, in order to adjust the distance of the substrate from the target. The internal of the

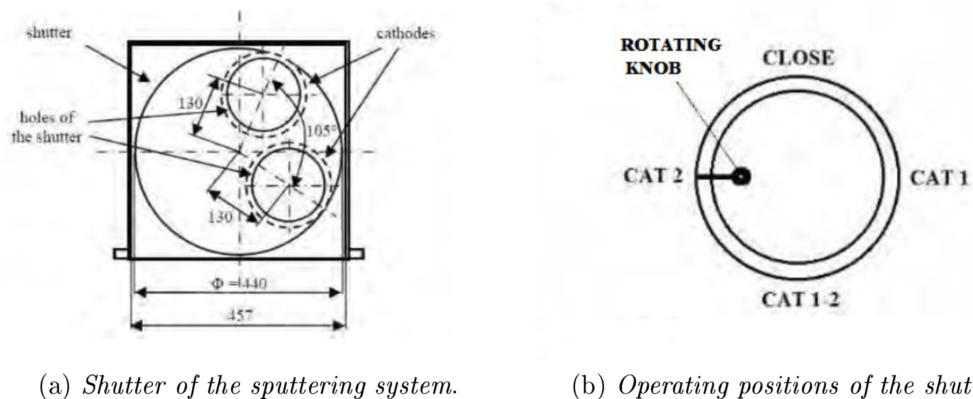

(a) *Shutter of the sputtering system.* (b) *Operating positions of the shutter.*

Figure 6.2: Shutter schematics [22]

Figure 6.3: Sputtering chamber

chamber and the disks can be seen in Fig. 6.3. The electrodes are made by a cylinder of copper, with the target above, as can be seen in Fig. 6.4. Under each electrode there are $NdFeB$ magnets to obtain the unbalanced configuration of type 2. The magnets are kept at room temperature by the cooling system (Tab. 6.5).
The characteristics of the cathodes are reported in Tab. 6.1

The pumping system is divided in two stages. The first stage is made by a rotary pump, which remains turned on also with the second stage. The second stage of the pumping system is composed by a turbomolecular pump. In Tab. 6.2 can be found the parameters of the rotary pump, while in Tab. 6.3 are listed the parameters of the turbomolecular pump.

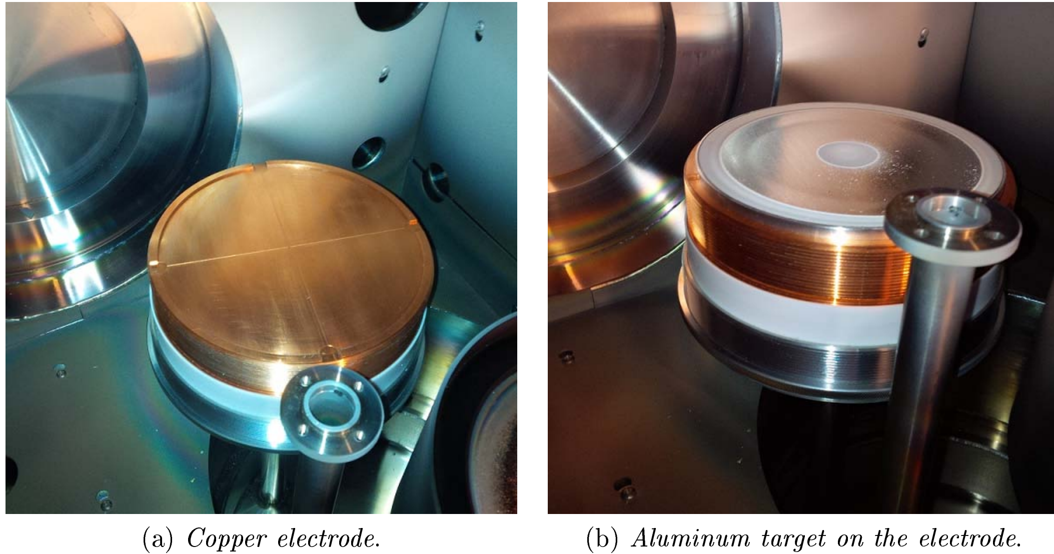

(a) *Copper electrode.* (b) *Aluminum target on the electrode.*

Figure 6.4: Electrode and target of the magnetron sputtering system

Model	Angstrom Science ONYX-6
Maximum power, DC sputtering	3 kW
Maximum power, RF sputtering	1kW
Shape of the target	Circular and Planar
Diameter of the target	6" $= 152,4mm$
Cooling system	Indirect
Magnets	NdFeB
Weight	9.97kg
External diameter	180.975mm

Table 6.1: Characteristics of the cathodes

Model	Leybold Trivac D 16 B
Flow rate	$16.5m^3/h$
Triphase motor	Koncar Mes $5AZ80B - 4$
Power of the motor	$750W$
Nominal velocity	$1500rpm$

Table 6.2: Characteristics of the rotary pump

Model	Pfeiffer TMU 261 P
Inlet flange	DN 100 CF-F
Outlet flange	DN 25 ISO-KF/G 1/4"
Flow rate for Ar	$200L/s$
Rotating speed	$60000rpm$
Cooling system	Water, Air

Table 6.3: Characteristics of the turbomolecular pump

Model	TruPlasma DC 4001
Input voltage	$3 \times 400V\ AC \pm 10\%$
Input current	$3 \times 2A$
Frequency	$50 - 60Hz$
Cooling system	Air
Pulsed feeding frequency	$2 - 100kHz$

Table 6.4: Characteristics of the feeding system

Model	Eurocold ACW-LP 12
Flow rate	$8 - 30L/min$
Power	$1500W$
Coolant	Water

Table 6.5: Characteristics of the cooling system

The Plasma is generated by a feeding system, made by TRUMPF HUTTINGER, whose characteristics are listed in Tab.6.4.

The cooling system, that operates with demineralized water, is made by Eurocold and the charactersitics can be seen in Tab. 6.5.

The magnetron sputtering system also has a protection system, designed to avoid any wrong operation. In particular, the turbomolecular pump can be switched on only if the pressure of the chamber is below a certain value and if the cooling system is on; the feeding system of the cathode can be turned on only if the chamebr door is closed and the cooling system is on and the emergency button allows to immediately turn off the whole system.

6.2 Realization of the Substrate

The piezoelectric cantilever is realized with a sequence of operations. The first operation is the cut of the metal sheet at the size of $70mm$ length and $15mm$ width. The second operation is to drill a $3mm$ hole near the end of the piece of metal, in order to screw the terminals of the signal cables. The following operation is the preparation of the substrate to be put into the sputtering system.

6.2.1 Preparation of the Substrate for the Deposition

The metal pieces of the substrate and the aluminum holders cannot be placed directly into the magnetron sputter. They need to be prepared, in order to remove

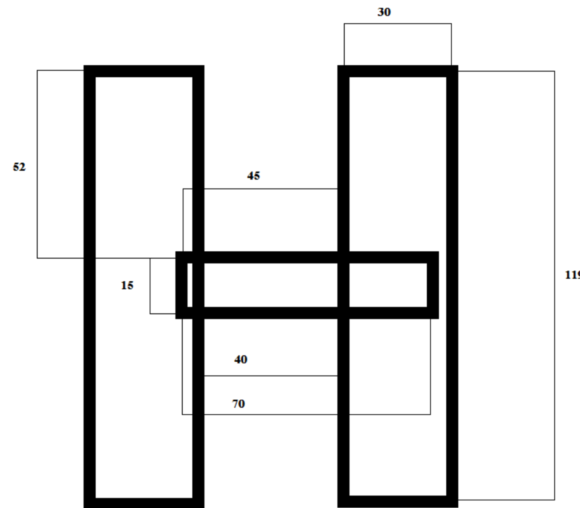

Figure 6.5: Position of the substrate on the aluminum holders

all the dirt particles that could interfere with the deposition.
Firstly, the aluminum holders of the substrate must be cleaned from the previous depositions in three steps

- removal of the previous deposition with medium sandpaper
- cleaning with acetone, to remove the largest particles of dirt and dust
- cleaning with alcohol, to remove fingerprints and small particles of dirt

The substrate is prepared in the same way, with the first step used to remove a thin oxide layer.
After the cleaning phase, the substrate can be placed on the aluminum holders. The length of the surface to be exposed to the magnetron sputtering is set to $40mm$, with a vibrating length of the cantilever of $45mm$. This means that the substrate is positioned as in Fig. 6.5 then it is fixed to the holders with a Kapton® adhesive tape. The substrate and the holders can be then placed into the chamber, with the substrate facing the electrode (Fig.6.6). After the correct positioning of the substrate the door of magnetron system can be closed and the rotary pump can be switched on. When the pressure is sufficiently low, usually $\sim 1 \times 10^{-2} mbar$ can be switched on also the turbomolecular pump.
The sputtering system is then pumped down to a base pressure lower than $1 \times 10^{-6} mbar$, which is a condition that has been chosen in order to operate with a completely cleaned system, since the steel of the walls tends to trap air and dust particles. These particles are released during the pumping down phase.
When the base pressure is sufficiently low, the Ar is admitted into the chamber, to start the pre-sputtering phase.

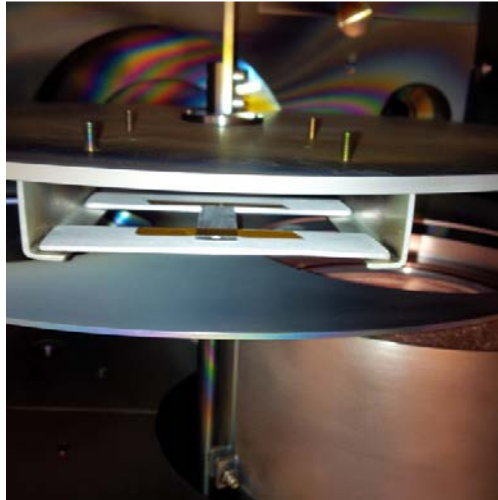

Figure 6.6: Positioning of the substrate and the holders into the chamber

6.2.2 Pre-sputtering Phase

The pre-sputtering phase is used to clean the target. During the opening of the sputtering system the target can be contamined with impurities or can face the formation of oxides on its surface. These impurities must be removed before the deposition phase.
This phase is performed with the shutter completely closed, in order to avoid the contamination of the substrate with impurities.
The parameters of the pre-sputtering phase are:

- DC pulsed at $50kHz$, with pause time of $2\mu s$ for each pulse period (of $20\mu s$)
- maximum power of $200W$
- maximum voltage of $800V$
- maximum current of $1500mA$
- Ar flow rate of $24sccm$ or $36sccm$
- pre-sputtering duration of $10'$

The pre-sputtering phase is followed by the sputtering phase, which is used to the thin film deposition. In this work the sputtering phase has been different for each substrate, therefore, each substrate is here described individually.

6.2.3 First Substrate

The first test has been done with a $0.3mm$ thick aluminum substrate. As the first test, the process parameters used has been chosen from previous work performed in the laboratory, on different substrates, e.g. glass and copper [23].
In particular the parameters during the deposition has been:

Time	Power $[W]$	Voltage $[V]$	Current $[mA]$	Pressure $[mbar]$
15”	600	294	2025	2.68×10^{-3}
$1'$	599	307	1945	2.69×10^{-3}
$2'$	599	312	1916	2.70×10^{-3}

Table 6.6: Aluminum nitride deposition, $Ar_{flow} = 12sccm$ and $N_{2,flow} = 12sccm$

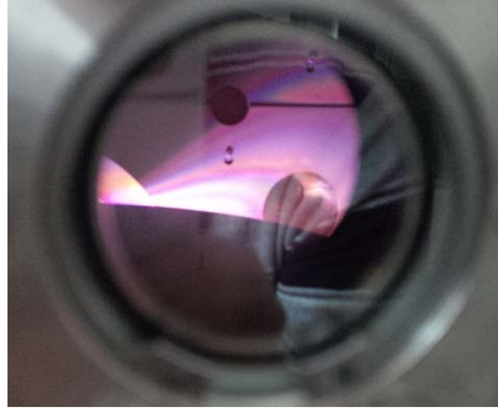

Figure 6.7: Glow discharge during the first deposition of AlN

- DC pulsed at $50kHz$, with with pause time of $2\mu s$ for each pulse period
- maximum power of $600W$
- maximum voltage of $800V$
- maximum current of $2250mA$
- Ar flow rate of $12sccm$
- N_2 flow rate of $12sccm$
- Al target, 99.999%
- sputtering duration of $3'$
- pressure during the deposition $2.95 \times 10^{-3}mbar$

In Tab. 6.6 has been collected the power, the voltage, the current and the pressure during the deposition. In Fig. 6.7 can be seen the glow discharge during the deposition.

At the end of the deposition, the feeding system is switched off, the inlet valves of argon and nitrogen are closed and the turbomolecular pump is turned off. When the turbomolecular pump stops the pressure into the chamber can be increased to the atmospheric pressure. In this way the door opens and the substrate can be

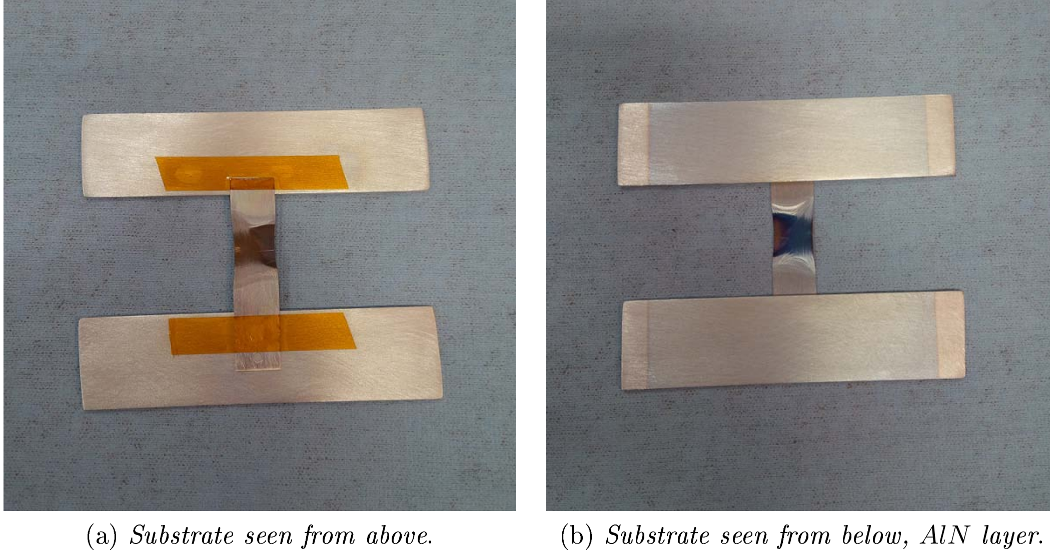

(a) *Substrate seen from above.* (b) *Substrate seen from below, AlN layer.*

Figure 6.8: The first substrate after $3'$ sputtering

Time	Power $[W]$	Voltage $[V]$	Current $[mA]$	Pressure $[mbar]$
15"	600	287	2076	2.58×10^{-3}
$1'$	599	301	1978	2.58×10^{-3}
$2'$	600	307	1945	2.58×10^{-3}

Table 6.7: Process parameters during the deposition of the second substrate

extracted.
The result of the first test showed that the thickness of the aluminum ($0.3mm$) were too small for the temperature reached on the substrate during the sputtering process, as can be seen in Fig. 6.8.
Due to the reduced thickness of the substrate in the central zone and its inhomogeneity, this substrate has not been used to realize a piezoelectric cantilever.
To prevent the damage of the substrate, the second test has been done on a $0.8mm$ thick aluminum substrate.

6.2.4 Second Substrate

The only difference on the realization of the second substrate from the previous test is the thickness; all the process parameter has been kept constant. Before the deposition phase, the substrate and the holders has been cleaned and placed as in Fig. 6.5 and then put into the chamber. Before the pre-sputtering phase, the pressure was below $1 \times 10^{-6} mbar$ and the pressure during the deposition has been kept equal to $3 \times 10^{-3} mbar$. The parameters during the deposition are shown in Tab.6.7.

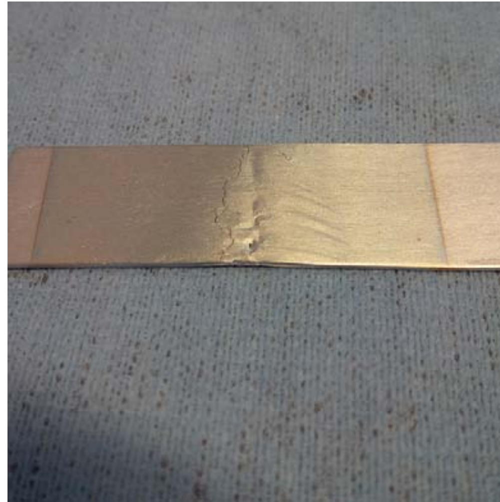

Figure 6.9: Holes on the second substrate

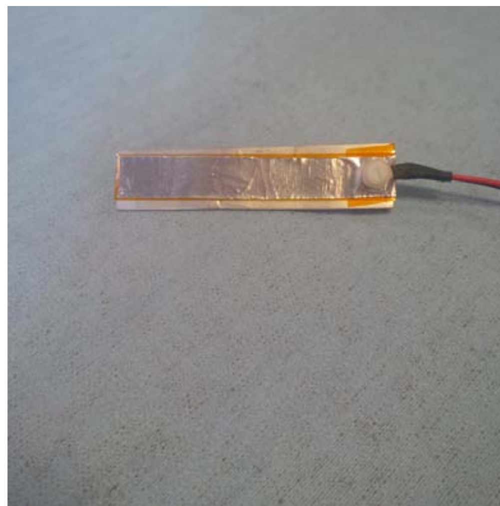

Figure 6.10: First piezoelectric cantilever

The result of the deposition, as can be seen in Fig. 6.9 was not yet satisfactory. There were holes in the center of the exposed zone with only $3'$ sputtering time, probably due to localized heating on the substrate during the glow discharge or the presence of low-melting impurities/ fusible alloyant. This substrate has been marked with one small adhesive label.

However, this second substrate has been used for the test assembly of the first piezoelectric cantilever energy harvester, realized as can be seen in Fig. 6.10.

6.2.5 Third Substrate

To avoid the same effect of the second substrate, the pressure is increased to $7 \times 10^{-3} mbar$, while the other process parameters are kept constant. In this way is possible to reduce the velocity of the particles impacting the substrate and increase

Time	Power $[W]$	Voltage $[V]$	Current $[mA]$	Pressure $[mbar]$
15"	600	297	1998	6.83×10^{-3}
$1'$	599	316	1897	6.87×10^{-3}
$2'$	600	321	1866	6.87×10^{-3}

Table 6.8: Parameters of the deposition on the third aluminum substrate

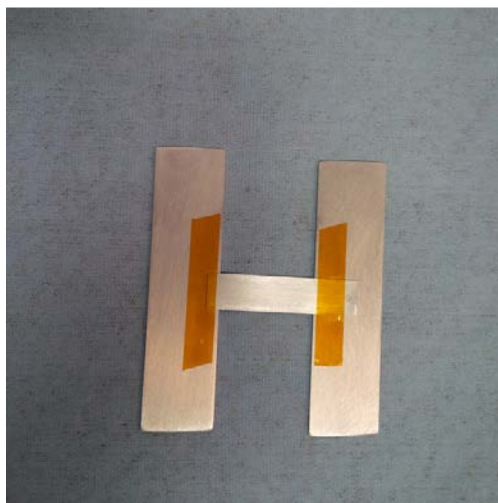

Figure 6.11: Third substrate, obtained at $p = 7 \times 10^{-3} mbar$

the homogeneity of the thin film. The flow rate of the Ar has been set to $10sccm$ and the flow rate of N_2 has been increased to $50sccm$.
The parameters during the deposition are shown in Tab 6.8.

With $3'$ deposition, the thickness of the layer should be lower than $1\mu m$ [23]. The result of the deposition can be seen in Fig. 6.11. This result is much more homogeneous than the one in Fig. 6.9. This substrate has been marked with two adhesive labels

6.2.6 Fourth Substrate

The main problem of the deposition on aluminum substrates is the low melting point of the aluminum and the use of aluminum alloys instead of pure aluminum sheets. A solution to this problem is the use of copper, whose melting point is at $1084°C$ instead of $660°C$ for Al and whose purity is above 99%, also for commercial Cu sheets. For these reasons the fourth deposition has been done on a copper sheet of $0.4mm$ of thickness.
After the cut and drill phase, the substrate has been cleaned and placed into the sputtering chamber. Then the pre-sputtering followed the reaching of the base pressure. Subsequently has been done the first deposition, with a different process with respect to the aluminum substrates.

Time	Power $[W]$	Voltage $[V]$	Current $[mA]$	Pressure $[mbar]$
15”	599	448	1341	4.62×10^{-3}
$1'$	599	442	1354	4.58×10^{-3}
$5'$	599	443	1354	4.62×10^{-3}
$8'$	599	443	1354	4.62×10^{-3}
$10'$	599	444	1352	4.62×10^{-3}
$14'$	599	444	1351	4.62×10^{-3}

Table 6.9: Parameters of the deposition of aluminum on the first copper substrate

Before the deposition of AlN, on the substrate has been deposited an aluminum interlayer with the following process parameters:

- DC pulsed at $50kHz$, with positive pulses of $2\mu s$
- maximum power of $600W$
- maximum voltage of $800V$
- maximum current of $2250mA$
- Ar flow rate of $36sccm$
- Al target, 99.999%
- sputtering duration of $15'$
- pressure during the deposition $4.62 \times 10^{-3} mbar$

The parameters recorded during the deposition of aluminum have been reported in Tab. 6.9.

The colour of the glow discharge during the deposition of aluminum, as can be seen in Fig. 6.12, is different from the colour of the glow discharge during the deposition of AlN.

The aluminum interlayer has the function to reduce the mismatch between the wurtzitic structure of the AlN and the Cu substrate, as shown by Akiyama et Al. [24].

After the deposition of the metallic interlayer, has been performed the deposition of AlN with the following process parameters:

- DC pulsed at $50kHz$, with positive pulses of $2\mu s$
- maximum power of $600W$
- maximum voltage of $800V$
- maximum current of $2250mA$

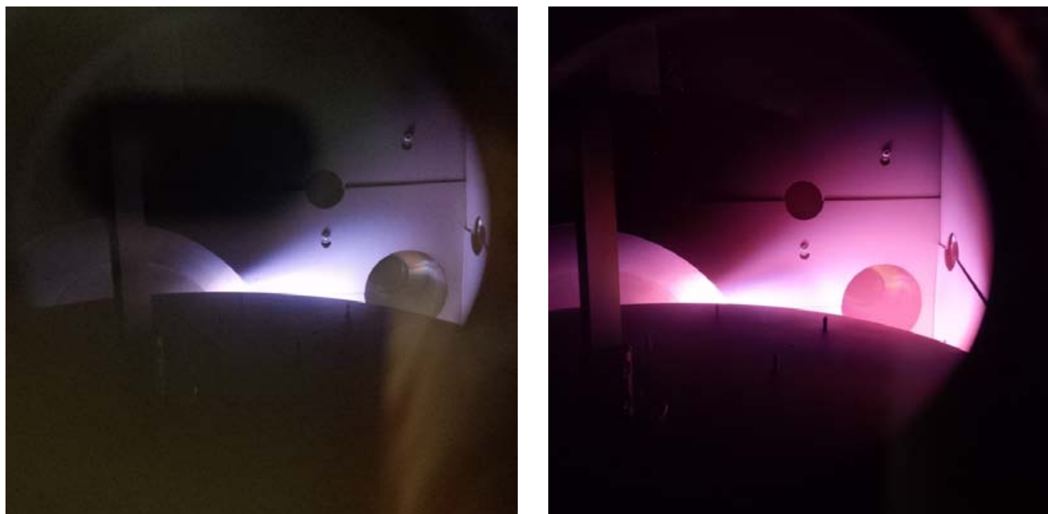

(a) *Glow discharge during the deposition of aluminum.* (b) *Glow discharge during the deposition of aluminum nitride.*

Figure 6.12: Different colours of glow discharge

Time	Power $[W]$	Voltage $[V]$	Current $[mA]$	Pressure $[mbar]$
15"	599	285	2102	6.74×10^{-3}
$2'$	599	312	1916	6.74×10^{-3}
$7'$	599	324	1849	6.83×10^{-3}
$13'$	599	327	1829	6.91×10^{-3}
$16'$	600	328	1826	6.95×10^{-3}
$18'$	599	328	1826	6.95×10^{-3}
$19'$	599	328	1826	6.95×10^{-3}

Table 6.10: Parameters of the deposition of aluminum nitride on the first copper substrate

- Ar flow rate of $10sccm$
- N_2 flow rate of $50sccm$
- Al target, 99.999%
- sputtering duration of $20'$
- pressure during the deposition $7 \times 10^{-3}mbar$

The parameters recorded during the deposition of aluminum nitride has been listed in Tab. 6.10

The first copper substrate has been marked with a single small adhesive label.

Time	Power $[W]$	Voltage $[V]$	Current $[mA]$	Pressure $[mbar]$
15"	599	442	1355	4.62×10^{-3}
$1'$	599	441	1357	4.62×10^{-3}
$3'$	599	442	1353	4.62×10^{-3}
$5'$	599	443	1352	4.66×10^{-3}
$11'$	599	443	1351	4.70×10^{-3}
$14'$	600	444	1351	4.70×10^{-3}

Table 6.11: Parameters of the deposition of aluminum on the second copper substrate

Time	Power $[W]$	Voltage $[V]$	Current $[mA]$	Pressure $[mbar]$
20"	599	283	2106	7.29×10^{-3}
$1'$	599	293	2032	decreased
$3'$	599	318	1883	6.91×10^{-3}
$5'$	599	322	1857	6.95×10^{-3}
$10'$	599	327	1833	6.99×10^{-3}
$15'$	599	330	1817	7.04×10^{-3}
$20'$	599	330	1816	7.08×10^{-3}

Table 6.12: Parameters of the first deposition of aluminum nitride on the second copper substrate

6.2.7 Fifth Substrate

Since one of the most important parameters of a piezoelectric cantilever is the thickness of the piezoelectric layer, the objective of the fifth substrate is to reach a thicker layer of piezoelectric material, but in order to do that, must be faced some problems.
The increase of temperature on the substrate is proportional to the time of the film thickness. Therefore to reach a thickness of the film of $\sim 2\mu m$, with an estimated growth of $25nm/min$ at $p = 7 \times 10^{-3} mbar$ and a maximum sputtering time of $15 \sim 20'$, four separate depositions have been used. An interval of a few hours (typically about $8h$) has been set between two following depositions, in order to ensure the cool down of the film and the substrate.
After the fourth AlN deposition, the turbomolecular pump has been switched off. Subsequently the substrate has been removed from the chamber, to be used as the main layer of the second copper-based cantilever, which can be recognised by two holes and two small adhesive labels.
The process parameters are set as in the case of the fourth substrate. The recorded values during the deposition of the first layer of aluminum can be seen in Tab 6.11, while the parameters during the four depositions of aluminum nitride can be seen in Tabs. 6.12,6.13,6.14 and 6.15.

Time	Power $[W]$	Voltage $[V]$	Current $[mA]$	Pressure $[mbar]$
15"	600	313	1922	6.95×10^{-3}
$1'$	599	316	1890	6.91×10^{-3}
$2'$	600	330	1812	6.91×10^{-3}
$4'$	599	337	1778	6.95×10^{-3}
$10'$	599	339	1767	6.99×10^{-3}
$14'$	600	338	1770	7.04×10^{-3}
$18'$	599	337	1777	7.04×10^{-3}
$19'$	599	336	1780	7.04×10^{-3}

Table 6.13: Parameters of the second deposition of aluminum nitride on the second copper substrate

Time	Power $[W]$	Voltage $[V]$	Current $[mA]$	Pressure $[mbar]$
15"	600	317	1894	6.95×10^{-3}
$1'$	599	321	1856	6.91×10^{-3}
$3'$	600	340	1762	6.91×10^{-3}
$9'$	600	343	1746	6.95×10^{-3}
$14'$	599	342	1750	6.99×10^{-3}
$15'$	599	342	1752	6.99×10^{-3}
$19'$	599	340	1763	7.04×10^{-3}

Table 6.14: Parameters of the third deposition of aluminum nitride on the second copper substrate

6.2.8 Sixth Substrate

In order to evaluate different process conditions on AlN made by different consecutive depositions, a sixth substrate has been prepared.

Time	Power $[W]$	Voltage $[V]$	Current $[mA]$	Pressure $[mbar]$
15"	599	320	1875	6.95×10^{-3}
$2'$	599	337	1771	6.87×10^{-3}
$5'$	599	345	1737	6.91×10^{-3}
$10'$	600	346	1734	6.95×10^{-3}
$15'$	600	344	1740	7.00×10^{-3}
$19'$	599	343	1747	7.04×10^{-3}

Table 6.15: Parameters of the fourth deposition of aluminum nitride on the second copper substrate

Time	Power $[W]$	Voltage $[V]$	Current $[mA]$	Pressure $[mbar]$
15"	599	440	1362	4.66×10^{-3}
$3'$	599	441	1359	4.66×10^{-3}
$6'$	599	442	1356	4.66×10^{-3}
$10'$	599	442	1354	4.66×10^{-3}
$13'$	599	442	1354	4.66×10^{-3}

Table 6.16: Parameters of the deposition of aluminum on the third copper substrate

Time	Power $[W]$	Voltage $[V]$	Current $[mA]$	Pressure $[mbar]$
30"	600	268	2222	4.95×10^{-3}
$1'30"$	599	280	2131	4.95×10^{-3}
$2'$	599	287	2084	4.95×10^{-3}
$4'$	599	290	2064	4.95×10^{-3}
$13'$	599	296	2020	4.99×10^{-3}
$14'$	600	297	2019	5.04×10^{-3}

Table 6.17: Parameters of the first deposition of aluminum nitride on the third copper substrate

To realize this substrate the pressure was decreased at $5 \times 10^{-3} mbar$. Since the reduction of pressure is related to an increase of the grow rate of the film, the time of the deposition is reduced from $20'$ to $15'$, while the process parameters of pre-sputtering and the sputtering of the aluminum interlayer were kept constant except for the flow rates of the gases, which were set to $36sccm$ of Ar for the pre-sputtering and the Al deposition and to $28sccm$ for Ar and $14sccm$ for N_2, with a resulting base pressure of $p_0 = 5.2 \times 10^{-3}$ for the four depositions of aluminum nitride. In this way the estimated grow rate is $\sim 33nm/min$.
After the fourth AlN layer the sputtering system has been turned off and the substrate, marked with two small adhesive labels, has been used to realize the third copper cantilever. The parameters recorded during the deposition of the aluminum layer are listed in Tab. 6.16, while the parameters during the four depositions of aluminum nitride are reported in Tabs. 6.17, 6.18, 6.19 and 6.20.

Time	Power $[W]$	Voltage $[V]$	Current $[mA]$	Pressure $[mbar]$
15”	600	288	2121	4.95×10^{-3}
$1'$	599	291	2055	4.91×10^{-3}
$4'$	599	302	1985	4.95×10^{-3}
$7'$	600	302	1980	4.95×10^{-3}
$11'$	600	302	1984	4.99×10^{-3}
$14'$	599	301	1990	4.99×10^{-3}

Table 6.18: Parameters of the second deposition of aluminum nitride on the third copper substrate

Time	Power $[W]$	Voltage $[V]$	Current $[mA]$	Pressure $[mbar]$
15”	599	286	2092	4.95×10^{-3}
$3'$	599	303	1975	4.95×10^{-3}
$7'$	599	305	1963	4.95×10^{-3}
$14'$	599	303	1977	4.99×10^{-3}

Table 6.19: Parameters of the third deposition of aluminum nitride on the third copper substrate

Time	Power $[W]$	Voltage $[V]$	Current $[mA]$	Pressure $[mbar]$
15”	600	313	1922	6.95×10^{-3}
$1'$	599	316	1890	6.91×10^{-3}
$2'$	600	330	1812	6.91×10^{-3}
$4'$	599	337	1778	6.95×10^{-3}
$10'$	599	339	1767	6.99×10^{-3}
$14'$	600	338	1770	7.04×10^{-3}
$18'$	599	337	1777	7.04×10^{-3}
$19'$	599	336	1780	7.04×10^{-3}

Table 6.20: Parameters of the fourth deposition of aluminum nitride on the third copper substrate

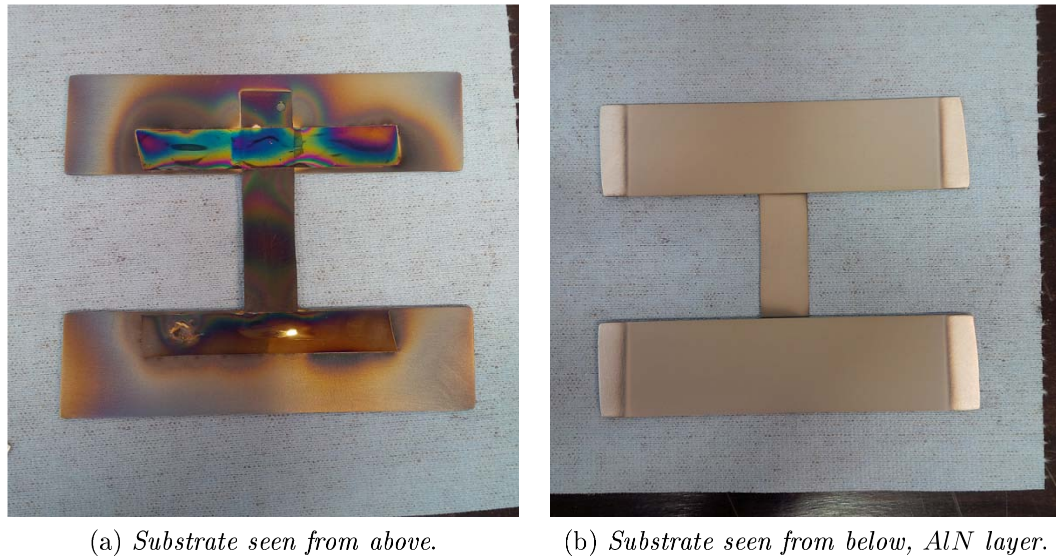

(a) *Substrate seen from above.* (b) *Substrate seen from below, AlN layer.*

Figure 6.13: Second copper substrate and aluminum holders after the depositions

6.3 Realization of the Cantilevers

All the substrates previously discussed were prepared in the same way, to realize a piezoelectric cantilever.
The substrate extracted from the chamber is fixed to the aluminum holders via adhesive tape, which must be removed after the deposition, as can be seen in Fig.6.13. Due to the reduced thickness of the AlN films and their inhomogeneity on these substrates, it seems not possible to make the deposition of the electrode directly on the piezoelectric layer, since it will short circuit the upper and the lower electrodes. For this reason on each substrate has been placed a piece of Kapton® adhesive tape, which guarantee the electrical insulation between the upper electrode and the piezoelectric material.
Since the width of the tape is lower than the width of the cantilever, the insulating layer is made in two steps, as can be seen in Fig. 6.14. The insulating layer then has to be drilled in corrispondence of the hole on the metal piece.
Subsequently the insulating layer is covered by an aluminum adhesive tape, previously cut $1mm$ narrower than the layer below. The tape is also drilled in correspondence of the hole on the other layers (Fig. 6.16). These operations are operated in order to ensure the electrical insulation between the electrodes. The hole in particular requires the absence of fringes. As a precaution a polyamide disk washer is placed in corrispondence of the hole, between the aluminum tape and the Kapton® tape.
The signal cables are connected to the electrodes with eyelet terminals and are screwed to the cantilever with a polyamide screw, as can be seen in Fig.6.17.
This procedure has been applied to the second and the third aluminum substrates and to all the copper substrates.

(a) *First piece of insulating tape.*

(b) *Second piece of insulating tape.*

Figure 6.14: Preparation of the insulating layer

Figure 6.15: Application of a Kapton® tape as insulating layer

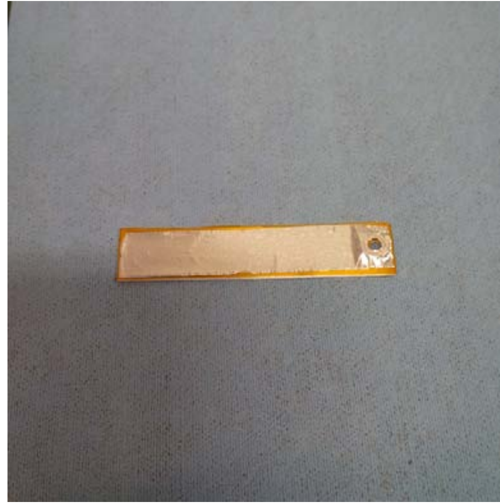

Figure 6.16: Second cantilever, made with the third substrate sputtered at $p = 0.7 \times 10^{-3} mbar$

Figure 6.17: Side view of the cantilever and the signal cables

Chapter 7

First Operation Tests

A part of the work for this thesis has been for the design and realization of a wooden support with a clamping system, in order to test each cantilever. On this system it is possible to generate vibrations on the cantilever by exerting a force on the support. The proximity of the human body could affect the signal measured on the electrodes of the cantilever due to electrostatic induction; the use of this support allow the avoidance of this effect.
The first version of the wooden support can be seen in Fig. 7.1 To reduce the torsion of the clamping system made with two glass-fiber reinforced polymer plates, the wooden support has been modified to a second version, that can be seen in Fig. 7.2. By doing so, the kinetic energy on the cantilever increases.

All the cantilevers have been tested, after being clamped on the wooden support, by connecting the signal cables to an oscilloscope. In the first test, has been used a simple oscilloscope, the Yokogawa $DL1540$ that can be seen in Fig. 7.3 and whose characteristics are listed in Tab.7.1.

To collect the data of the cantilevers tested, has been used also another oscilloscope, the Yokogawa $DL9140$, that can be seen in Fig.7.4 and whose characteristics

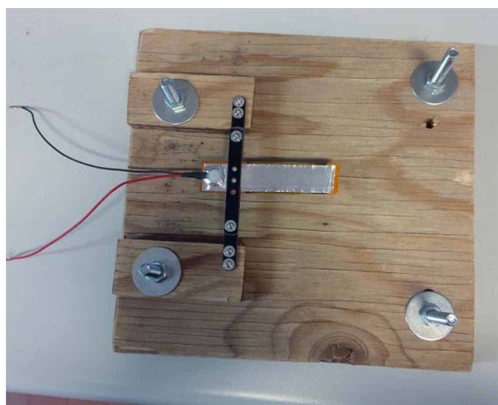

Figure 7.1: First version of the wooden support

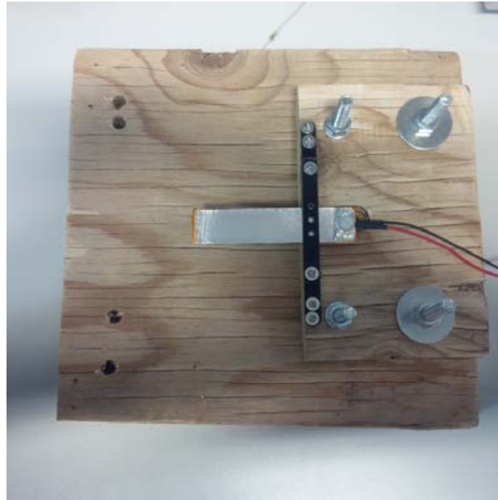

Figure 7.2: Second version of the wooden support

Producer	YOKOGAWA
Series	DL1540
Model	501710
Max sampling rate	$200MS/s$
Analog frequency bandwidth	$150MHz$
Input channels	4
Input impedance	$1M\Omega \sim 25pF$

Table 7.1: Characteristics of DL1540 oscilloscope [25]

Figure 7.3: Yokogawa digital oscilloscope $DL1540$

Producer	YOKOGAWA
Series	DL9140
Model	710310
Max sampling rate	$5GS/s$
Analog frequency bandwidth	$1GHz$
Input channels	4
Input impedance	$1M\Omega \sim 20pF$ $10M\Omega \sim 14pF$ 50Ω

Table 7.2: Characteristics of DL9140 oscilloscope [25]

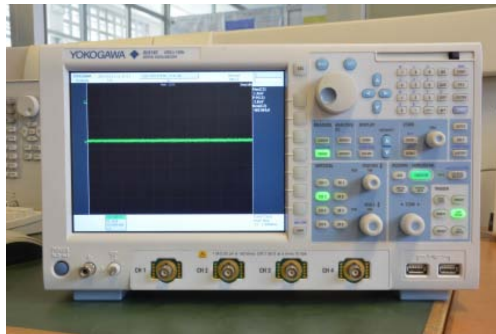

Figure 7.4: Yokogawa digital oscilloscope $DL9140$

are listed in Tab. 7.2. This oscilloscope allows the export of data via USB drive.

The first test has been done with the cantilever realized on the second aluminum substrate.The thickness of the piezoelectric layer has been hypothesized to be $\sim 100nm$, by using the results of a previous work [23] where, with the same process conditions, the growth rate was $35nm/min$.
The main problem of this substrate is the presence of a crack and several holes at the middle of the length of the cantilever. However, this cantilever has been clamped on the support and connected to the oscilloscope $DL1540$. By hitting the wooden support it is possible to simulate a rudimentary impulsive vibrations system. The result has been recorded on the oscilloscope, as can be seen in Fig. 7.5. This cantilever shows a sinusoidal background noise with a $Vpp \simeq 20mV$. With a pulse applied to the support, it has been obtained a $V_{pp} = 120mV$ and it is possible to see the damped response of the system. The resonance frequency, which results to be $\sim 50Hz$, is lower than one half of the estimated frequency, previously reported of about $122Hz$. This could be related to the crack and the holes in the middle of the substrate and a poor clamping stiffness on the first wooden support.
After the deposition of aluminum nitride on the third substrate, which has been performed at higher pressure, the second cantilever has been realized and clamped

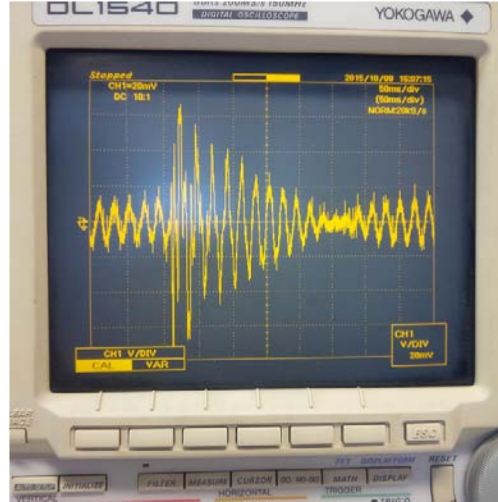

Figure 7.5: Voltage measured on the first cantilever. The sinusoidal wave is the background noise

on the support, to be tested.
The result of the test can be seen in Fig. 7.6. This cantilever, after the application of a pulse on the wooden support, shows only a small $\Delta V \simeq 20mV$, which is barely higher than the background noise.
The second part of the test campaign has been performed on the copper-based cantilevers.
The first copper cantilever has only one deposition of aluminum nitride, for an estimated thickness of $460nm$, calculated with a growth rate of $23nm/min$ [23] and a duration of the deposition of $20'$.

In this case the measured frequency is $\sim 83Hz$, which is the 30% less than the theorical resonance frequency and the maximum voltage measured is $V_{pp} \simeq 140mV$.
To increase the voltage generated by the cantilever, have been realized the fifth and the sixth substrates with an estimated thickness of the aluminum nitride film of $2\mu m$. The thickness of the piezoelectric layer is infact related to the voltage measured on the electrodes of the cantilever. In particular, from the work of Stoppel et al. [26] it is possible to express the generated voltage on a load resistance R:

$$U = \frac{j\omega d_{31}\beta m_{eff} awlKh_f R}{(j\omega d_{31}^2 wlKE + (j\omega K - j\omega^3 m_{eff} - \omega^2\zeta)h_p C_p)R + (K - \omega^2 m_{eff} + j\omega\zeta)h_f} \tag{7.1}$$

where β is a geometric parameter, m_{eff} is the effective mass, K is the stiffness, and C_p is the piezoelectric capacitance.

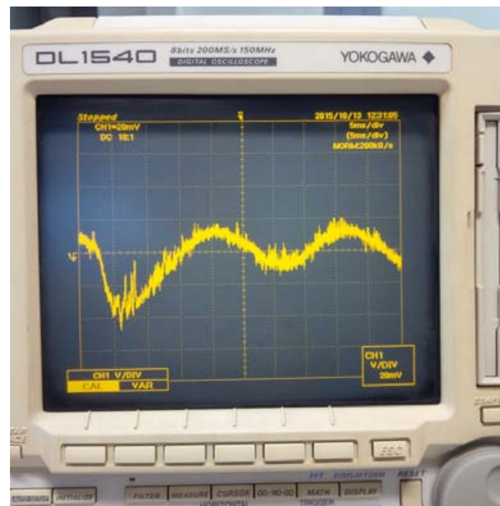

Figure 7.6: Voltage measured on the second aluminum based cantilever. The sinusoidal wave is the background noise

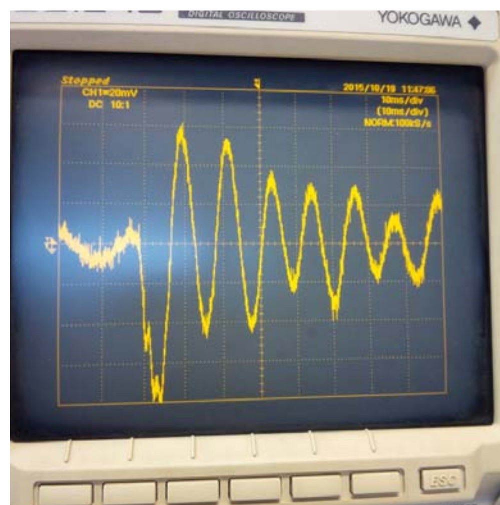

Figure 7.7: Voltage measured on the first copper based cantilever

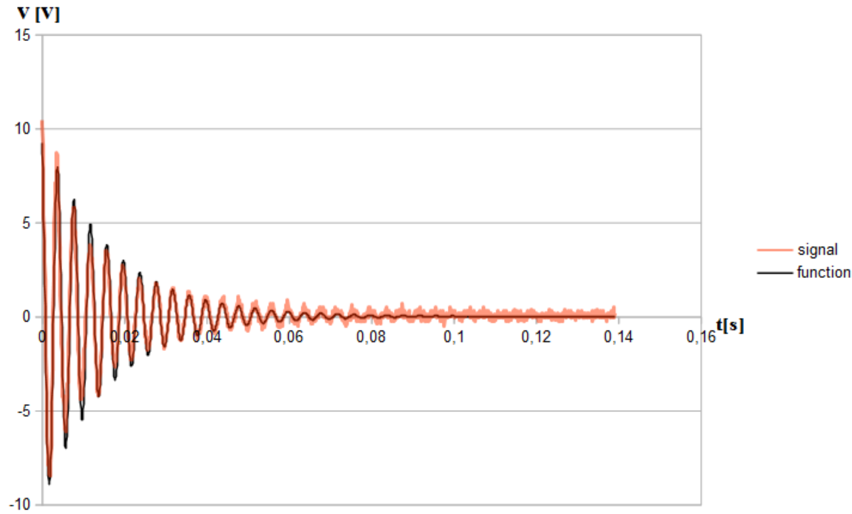

Figure 7.8: Recorded signal of a commercial cantilever

7.1 Test of a Commercial Cantilever

Before the analysis of the cantilevers realized in the laboratory, there was the need to have a comparative case, with well known parameters. For this reason has been tested a commercial cantilever made by *Midè Technologies*, the Energy Harvester Volture $V21B$ [21].
The nominal resonance frequency of this cantilever, without tip mass is $f = 275Hz$. This device has been clamped on its wooden support and then has been tested. The cantilever was connected to the oscilloscope $DL9140$, then a pulse has been applied to the support. The signal produced has been recorded and subsequantly analyzed, as can be seen in Fig. 7.8. The recorded signal has been suppose to be in the form of

$$x(t) = e^{-\zeta\omega_n t}[Ccos(\omega_n\sqrt{1-\zeta}t + \phi)] \tag{7.2}$$

Therefore on a spreadsheet software the data has been processed and, by the means of an equation solver, has been calculated the parameters of the Eq. 7.2, that are

- $C = 10V$
- $\zeta = 0.038$
- $f = \frac{\omega_n}{2\pi} = 255Hz$
- $\phi = \frac{\pi}{6}$

7.2 Analysis of the Second and Third Copper-based Cantilever

The four aluminum nitride depositions of the second copper-based cantilever has been performed at $7 \times 10^{-3} mbar$. After the realization phase, this cantilever has

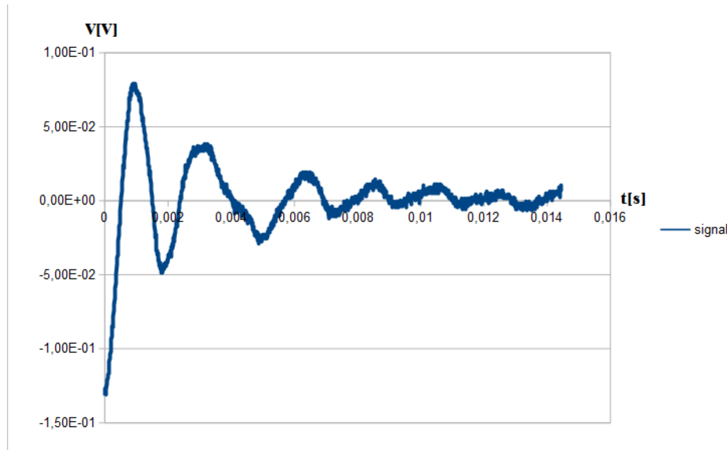

Figure 7.9: Recorded signal of the second copper-based cantilever

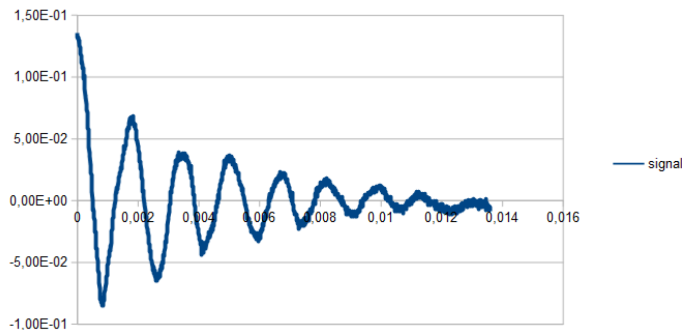

Figure 7.10: Recorded signal of the third copper-based cantilever

been tested on the second version of the wooden support.
The signal generated by this cantilever is reported in Fig.7.9.

The experimental data show a maximum $V_{pp} \simeq 200mV$, with a frequency $f \simeq 450Hz$.
On the third copper substrate the depositions of aluminum nitride has been performed at $5 \times 10^{-3}mbar$. This cantilever, as for the previous one, after the realization phase, has been clamped on the support and subsequently tested.
The signal cables were connected to the Yokogawa $DL9140$ to collect the data of the operation test.
The signal generated by the cantilever is reported in Fig. 7.10. The experimental data show a maximum $V_{pp} \simeq 210mV$, with a frequency $f \simeq 600Hz$.

The signals have been obtained trying to have the same pulse on the wooden support.
With respect to the first copper-based cantilever, signals with hicher peak have been obtained. A high value for the fundamental frequency has been observed, that, in part is due to the composite structure of the cantilever as shown, in a preliminary way, with the numerical analysis performed with COMSOL® Multi-

physics and reported at the end of Section 5.
Another aspect to be analyzed is the non ideal surface of the adhesive tapes.

Chapter 8

Conclusions

In this thesis work the feasibility of piezoelectric kinetic energy harvesters by the means of aluminum nitride, i.e. the feasibility of a lead-free piezoelectric cantilever, has been shown.
In particular the cantilevers realized with aluminum nitride sputtered in the range $4 - 5 \times 10^{-3} mbar$ showed the best behavior from the point of view of the obtained voltage peak.
Cantilevers with a substrate in commercial aluminum and copper have been realized, and the best results have been obtained by using copper as substrate.
In particular further development could be achieved with an investigation on the effect of the insulating interlayer between the aluminum nitride layer and the upper electrode. A reduction of its thickness has to be investigated.
Another important issue is the mechanical characterization of the cantilever systems by the means of a vibration system to exert vibration waves of different frequencies, with the measure of the induced acceleration in order to compare performances of the obtained cantilevers.

Bibliography

[1] J. Zhou, M. DeMiguel-Ramos, L. Garcia-Gancedo, E. Iborra, J. Olivares, H. Jin, J. K. Luo, A. S. Elhady, S. R. Dong, D. M. Wang, and Y. Q. Fu. Characterization of aluminium nitride films and surface acoustic wave devices for microfluidic applications. *Sensors and Actuators B: Chemical*, 202, 2014.

[2] S. V. Danylyuk, R. Ott, G. Panaitov, G. Pickartz, E. Hollmann, S. A. Vitusevich, A. E. Belyaev, and N. Klein. Aluminium nitride-niobium multilayers and free-standing structures for MEMS. *Thin Solid Films*, 515, 2006.

[3] S. Petroni, C. La Tegola, G. Caretto, A. Campa, A. Passaseo, M. De Vittorio, and R. Cingolani. Aluminium Nitride piezo-MEMS on polyimide flexible substrates. *Microelectronic Engineering*, 88, 2011.

[4] A. T. Tran, G. Pandraud, H. Schellevis, T. Alan, V. Aravindh, O. Wunnicke, and P. M. Sarro. Fabrication of AlN slender piezoelectric cantilevers for high-speed MEMS actuations. *Procedia Engineering*, 25, 2011.

[5] M. Fiorindo. Influence of vibrations and magnetic fields on single crystal growth. Bachelor thesis, Università di Padova, February 2013.

[6] D. Desideri. Electrical and Electromagnetic micro/nano devices. Notes of the 2013/2014 Course. Università di Padova.

[7] D. Hestenes and J. Holt. Crystallographic space groups in geometric algebra. *Journal of Mathematical Physics*, 48, 2007.

[8] M. Guglielmi. *Dispense di Scienza e tecnologia dei materiali ceramici*. Libreria Progetto, 2014.

[9] L. E. Cross and R. E. Newham. *History of Ferroelectrics*. The American Ceramic Society, Inc., 1987.

[10] W. Cady. *Piezoelectricity: An introduction to the theory and application of electromechanical phenomena in crystals*. Dover Pubblications, 1964.

[11] D.J. Griffiths. *Introduction to Electrodynamics*. Pearson Education, 2014.

[12] F.E. Neumann. *Vorlesungen über die Theorie der Elastizität der festen Körper und des Lichtäthers*. Teubner, 1885.

[13] www.token.com. Dielectrics, piezoelectrics, pyroelectrics, ferroelectrics, 2015. [Accessed on 11/11/2015].

[14] K. Dovidenko, S. Oktyabrsky, J. Narayan, and M. Razeghi. Aluminum nitride films on different orientations of sapphire and silicon. *Journal of Applied Physics*, 79, 1996.

[15] M. A. Dubois and P. Muralt. Stress and piezoelectric properties of aluminum nitride thin films deposited onto metal electrodes by pulsed direct current reactive sputtering. *Journal of Applied Physics*, 89, 2001.

[16] J. Wang, W. L. Wang, P. D. Ding, Y. X. Yang, Fang. L., J. Esteve, M. C. Polo, and G. Sanchez. Synthesis of cubic aluminum nitride by carbothermal nitridation reaction. *Diamond and Related Materials*, 8, 1999.

[17] http://semipark.co.kr. Thin film deposition, 2015. [Accessed on 15/11/2015].

[18] G. Santagiuliana. Synthesis and characterization of TiC and TiC/a-C:H nanocomposites using DC magnetron sputtering and high power magnetron sputtering. Master's thesis, Università degli studi di Padova, 2011.

[19] G. Serianni and P. Sonato. Industrial plasma technology. Notes of the 2013/2014 Course. Università di Padova.

[20] Slovak academy of Science. Magnetron sputtering configuration, 2015. [Accessed on 16/11/2015].

[21] M. Poggeschi Belloni. Realizzazione e caratterizzazione di film in nitruro di alluminio e prove di funzionamento di un cantilever commerciale. Master's thesis, Università degli studi di Padova, 2014.

[22] R. Dal Santo. Realizzazione di film sottili in nitruro di alluminio. Master's thesis, Università degli studi di Padova, 2015.

[23] D. Desideri, T. Cavallin, A. Maschio, and M. PoggeschiBelloni. Aluminium nitride films on glass. In *Nanotechnology Materials and Devices Conference (NMDC), 2014 IEEE 9th*, Oct 2014.

[24] M. Akiyama, K. Nagao, N. Ueno, H. Tateyama, and T. Yamada. Influence of metal electrodes on crystal orientation of aluminum nitride thin films. *Surface Engineering, Surface Instrumentation and Vacuum Technology*, 74, 2004.

[25] Yokogawa Electric Corporation. Digital oscilloscope specifications, 2015. [Accessed on 22/11/2015].

[26] F. Stoppel, C Schroder, F. Senger, B. Wagner, and W. Benecke. AlN-based piezoelectric micropower generator for low ambient vibration energy harvesting. *Procedia Engineering*, 25, 2011.